TRANSPORT AND DYNAMICS IN SUPERCOOLED CONFINED WATER

FRANCESCO MALLAMACE,[1,2] CARMELO CORSARO,[2]
SOW-HSIN CHEN,[1] and H. EUGENE STANLEY[3]

[1]*Dipartimento di Fisica and CNISM, Università di Messina, I-98166 Messina, Italy*
[2]*Department of Nuclear Science and Engineering, Massachusetts Institute of Technology, Cambridge, MA 02139, USA*
[3]*William Fairfield Warren Distinguished Professor; Professor of Physics; Professor of Chemistry; Professor of Biomedical Engineering; Professor of Physiology, Center for Polymer Studies, Department of Physics, Boston University, Boston, MA 02215, USA*

CONTENTS

Liquid Polymorphism: Advances in Chemical Physics, Volume 152, First Edition.
Edited by H. Eugene Stanley.

I. INTRODUCTION

Water in its several forms is the substance most essential to life on earth. Some of its crystalline forms are stable in certain temperature–pressure ranges and others are metastable. Although the stable form of water at sufficiently low temperatures is crystalline, inside this stable phase, water can also exist in liquid form. When this occurs, water is said to be supercooled. Supercooled water occurs naturally in the form of small droplets in clouds. If liquid water is cooled quickly enough, the crystalline phase can be bypassed and a noncrystalline (amorphous) solid, that is, a glass, is the result. This amorphous glass phase of water is polymorphic, that is, it can exists in two different forms. Glassy water is undoubtedly the most common form of water in the universe. Scientists puzzle over the anomalous properties of glassy water: when it is cooled it becomes more compressible, when compressed it is less viscous, and when cooled sufficiently, it expands.

Despite the many centuries of research on water and water-based systems, its unusual properties, anomalous when compared to "normal" liquids, are far from being understood [1]. In current research, there are several active problems of fundamental interest concerning the relevant chemistry and physics of water. Among these are the anomalies exhibited by water in its thermodynamic response functions, the localization (or the existence) of its glass transition (GT), the way in which it forms a glass and, when in a pure substance, the existence of a second critical point. Our study of the anomalies of water below its melting temperature focuses on its metastable states, that is, its supercooled regime and its two glassy states. Although water is generally associated with bulk water—for example, oceans, lakes, rivers, reservoirs, or aqueducts—our focus is on confined water, that is, water located on surfaces and little cavities thus in microscopic or mesoscopic structures.

The first anomalous property of liquid water was observed about 330 years ago [2]. Although most liquids contract as temperature decreases, liquid bulk water begins to expand when its temperature drops below 277K. Indeed, a simple kitchen experiment demonstrates that the bottom layer of a glass of unstirred iced water remains at 277K while colder layers of 273K water float on top. The anomalous properties of liquid bulk water become more pronounced in the supercooled region below the melting temperature, $T_{\mathrm{m}} = 273\mathrm{K}$ [2,3].

A salient characteristic of liquid water at ambient pressure is that its thermodynamic response functions (response of density ρ or of the entropy S to changes in temperature T or pressure P) sharply increase in magnitude upon cooling. As shown in Fig. 1, the increase begins at 319K for the isothermal compressibility (Fig. 1a) $K_T = (\partial \ln \rho / \partial \ln P)_T$, at 308K for the isobaric specific heat (Fig. 1b) $C_p = T(\partial S/\partial T)_p$, and at 277K for the magnitude of the thermal expansion coefficient (Fig. 1c) $\alpha_p = -(\partial \ln \rho / \partial T)_p$. In particular, while the anomalies displayed by liquid water are apparent above T_{m}, they become more striking as one supercools

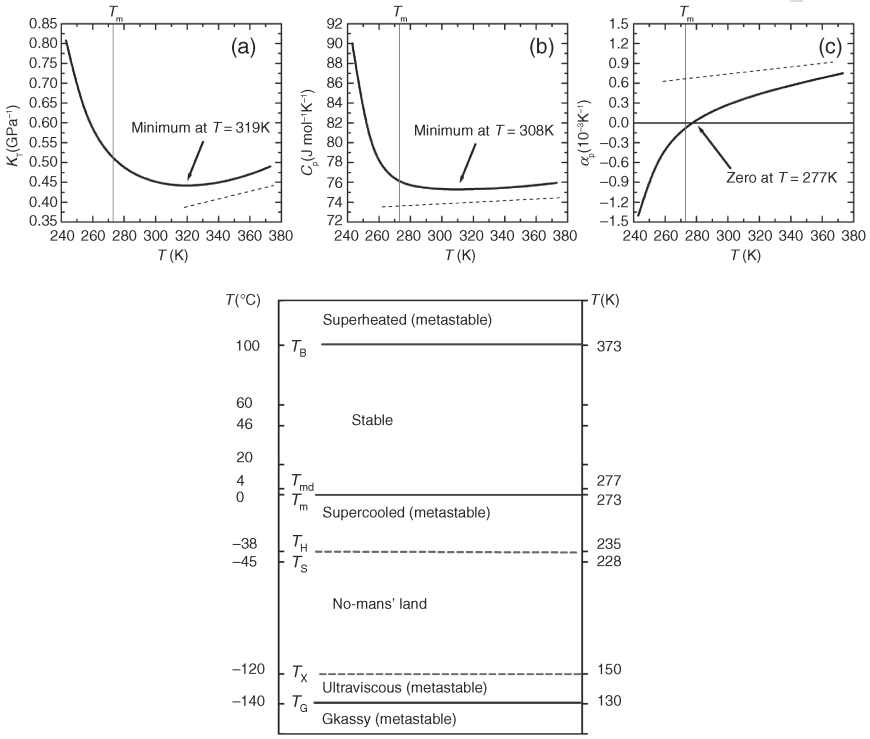

Figure 1. Examples of water's thermodynamic anomalies. Dependence on temperature of **(a)** the isothermal compressibility K_T, **(b)** the isobaric specific heat C_p, and **(c)** the coefficient of thermal expansion α_p. The behavior of water is indicated by the solid line; that of a typical liquid by the dashed line. Data from Ref. [5]. Bottom: Schematic illustration of different temperature domains, at atmospheric pressure, of H_2O. Only one domain is stable; the others are metastable.

below T_m. In fact, extrapolated from their values at moderately supercooled states, below the lowest temperatures measurable, all these functions appear to diverge at a singular temperature around $T_S = 228$K [4].

Each thermodynamic response function is associated with microscopic fluctuations: $K_T = \langle(\delta V)^2\rangle / k_B TV$ is proportional to volume (or density) fluctuations (δV) and C_p to the entropy fluctuations (δS) at fixed pressure: $C_p = \langle(\delta S)^2\rangle / k_B$ whereas $\alpha_p = \langle \delta S \delta V\rangle / k_B TV$ reflects the S and V cross-correlations. In typical liquids, V and S fluctuations become smaller as the temperature decreases. In water, the fluctuations of these quantities become more pronounced as the temperature decreases. δV and δS in most liquids are positively correlated: an increase in volume results in a corresponding increase in entropy, instead in water for

$T < 277$K, are anticorrelated, thus an increase in volume brings about a decrease in entropy.

These anticorrelations become increasingly pronounced in the supercooled state of water. Their microscopic origin lies in the tetrahedral symmetry in the local ordering of the molecules. This ordering is driven by a hydrogen bonding (HB) interaction that is a noncovalent interaction between an electropositive hydrogen atom on one molecule and an electronegative oxygen atom on another molecule. Thus, in ordinary ice each water molecule has four nearest neighbors and acts as a hydrogen donor to two of them and a hydrogen acceptor for the other two. Unlike ice, which is a permanent tetrahedral network held together by hydrogen bonds, the tetrahedrality of liquid water is local and transient. Regions of local tetrahedral order possess a larger specific volume than the average specific volume—unlike a region of, for example, local close-packed order. On the other hand, the entropy always decreases on cooling because the specific heat is, of necessity, positive. As T decreases, the local specific volume increases due to the progressive increase in tetrahedral order. Thus, the entropy and volume can become anticorrelated, and α_p can become negative. This is also a property of other liquids with local tetrahedral symmetry, such as silica.

When water is sufficiently cold, its diffusivity increases and its viscosity decreases upon compression. Pressure disrupts the tetrahedral HB network, and the molecular mobility consequently increases. In contrast, compression of most other liquids leads to a progressive loss of fluidity as molecules are squeezed closer together. The anomalous pressure dependence of water's transport coefficients [2,3] occurs below ≈ 306K for the viscosity and below ≈ 283K for the diffusivity, and persists up to pressures of around 2 kbar. Recent studies on diffusion show that, as T approaches the supercooled region, motion becomes increasingly complex. Simulations in particular show that during a randomly selected picosecond time interval, most water molecules are confined or "caged" by the HB network [6]. Only a small fraction of the caged molecules is able to break out of their cages. Rather than being isolated, these newly freed molecules appear to form clusters not altogether unlike the dynamic heterogeneities that are believed to be distinguishing features of supercooled liquids in general [2]. Thus in the supercooled state water is both spatially and dynamically heterogeneous.

Figure 1 (bottom) is a schematic illustration of the different temperature domains of H_2O at atmospheric pressure. One domain is stable; the others are metastable. All the indicated values are experimentally observed, except T_S, a fitting parameter that emerges by assuming the singular behavior proposed for K_T [4]. The region between the homogeneous nucleation curve $T_H(P)$ and the crystallization curve $T_X(P)$ is a kind of "No-Man's Land," as experiments on the liquid phase cannot be performed. The temperatures denoted 60, 46, 20, and 4°C indicate the onset of anomalies in the sound velocity, isothermal compressibility,

shear viscosity, and density, respectively. T_B is the boiling temperature and T_g is the GT temperature. Water can also exists in a glassy form at the lowest temperatures. Depending on T and P, water has two amorphous (glassy) phases with different structures—low-density amorphous (LDA) and high-density amorphous (HDA) ice—and thus exhibits polyamorphism. LDA can be formed from HDA and vice versa. If LDA is heated it first undergoes a glass-to-liquid transition into a highly viscous fluid and then, at $T_X = 150$K, crystallizes into cubic ice [7,8].

Water, like any liquid, can be heated above its boiling point without undergoing a phase transition. The attainable temperature, which is controlled by the nucleation rate, is ~ 553K. At atmospheric pressure it is possible to supercool water to its homogeneous nucleation temperature $T_H \approx 231$K, at which the nucleation rate suddenly becomes very large. Thus, the temperature range over which water can exist as a liquid (231–553K) is more than three times larger than the normal stability range (273–373K). Limits of supercooling or superheating, being kinetic in nature, are not absolute and can be bypassed if the observation time is shorter than the nucleation time.

An experimentally inaccessible T region exists in bulk water between T_H and T_X. This interval between the glassy and liquid phase is a frontier domain whose experimental exploration is key to a full understanding of metastable water. The observation of liquid bulk water in this experimental range is challenging regardless of whether one attempts to enter the No-Man's Land by cooling liquid water or by heating glassy water [3]. Supercooling is challenging because the nucleation time becomes extremely short below T_H. In the 140–150K range, the extremely large viscosity causes the nucleation rate to slow down. In principle this allows a much longer observation time, but when glassy water is heated it crystallizes at about 150K (T_X).

Because glasses are nonequilibrium materials, their physical properties depend on the process used to make them and, in principle, different glassy forms can be obtained by following different preparation protocols. It is thus not surprising that water can have different glassy phases. However, water is unusual in that the transformation between different forms can be sharp and reversible and is accompanied by large changes in fundamental physical properties such as the density, a behavior suggestive of a thermodynamic phase transition. Two forms of glassy water, which correspond to two different local tetrahedral arrangements, have been studied extensively: LDA [9] and HDA [7] ice. HDA has a structure similar to that of high-pressure liquid water, suggesting that HDA may be a glassy form of high-pressure water [10], just as LDA may be a glassy form of low-pressure water. Water has, thus, at least two different amorphous solid forms, a phenomenon called *polyamorphism* [8,11], and recently additional forms of glassy water have been the focus of active experimental and computational investigations [12–14], for example, very high-density amorphous ice (VHDA) [12]. The glassy states differ

in structure as revealed by neutron scattering, X-ray diffraction (XRD), and Raman spectroscopy, and in thermodynamic properties such as density. Different routes to the formation of glassy water are possible. HDA is formed by the pressure-induced amorphization of ordinary ice (ice I_h), the compression of LDA, the rapid cooling of emulsified liquid water at high pressure, or the constant-volume (isochoric) heating of VHDA. LDA is formed by rapidly cooling water vapor or liquid water after annealing. It is also formed by heating decompressed HDA or VHDA. VHDA is formed by annealing HDA at high pressure. All of these processes are irreversible. A reversible technique is the transformation between LDA and HDA by pressure cycling at about 135K and 2 kbar.

The commonly accepted value for water's GT temperature at ambient pressure is $T_g = 136$K (assigned to the LDA glass transition). Increasing the temperature leads to the formation of an extremely viscous liquid water and the crystallization to cubic ice at 150K. An alternative and controversial hypothesis is that T_g is located at a different temperature value [15]. Due to the importance of this subject, we will discuss the T_g location and its interpretation in a next section.

II. CURRENT HYPOTHESES

Many classic "explanations" for the behavior of liquid bulk water have been developed [16–18]. A truly coherent picture of the thermodynamics of metastable water should make clear (a) the anomalous behavior of the thermodynamic parameters in the supercooled region, (b) the properties and nature of the transition between the two glassy phases LDA and HDA, and (c) the relationship between supercooled and glassy water.

Three hypotheses attempting to rationalize these experimental observations are under current discussion:

(i) The *stability limit conjecture* [19], which assumes that the spinodal temperature line $T_{sp}(P)$ between two liquids with different densities in the pressure–temperature (P–T) phase diagram connects at negative P to the locus of the liquid-to-gas spinodal for superheated bulk water. Liquid water cannot exists when cooled or stretched beyond the line $T_{sp}(P)$.

(ii) The *singularity-free scenario* [20], which considers the possibility that the observed polyamorphic changes in water resemble a genuine transition, but are not. For example, if water is a locally structured transient gel comprised of molecules held together by HBs whose number increases as temperature decreases [21,22], then the local "patches" or bonded sub-domains [23,24] lead to enhanced fluctuations of specific volume and entropy and of their negative cross-correlations whose anomalies closely match those observed experimentally. In this scenario, the amorphous states are the corresponding vitreous forms of the LDL and HDL. Upon supercooling, the response

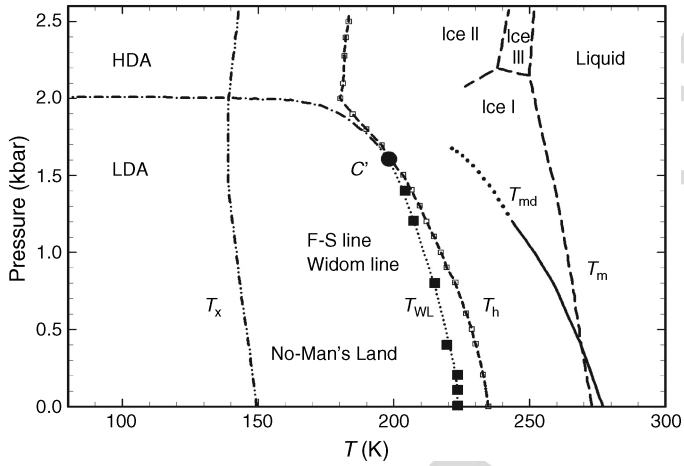

Figure 2. The phase diagram of water in the P–T plane [2,3]. T_H denotes the homogeneous nucleation temperature line, T_X is the crystallization line of amorphous water, T_m is the melting temperature line, and T_{md} is the maximum density line. T_W indicates the Widom line locus.

functions increase sharply but remain finite displaying pronounced maxima with respect to temperature. The transition between LDA and HDA is continuous. Because sharp maxima in the response functions imply large changes in entropy and volume, the transition between LDA and HDA is predicted to occur in a narrow interval of temperature and pressure that is difficult to distinguish experimentally from a true line when glassy phases are involved.

(iii) The *LLPT hypothesis* [25] arose from MD studies on the structure and equation of state of supercooled bulk water. According to this model, the transition between LDA and HDA is a low-temperature manifestation of a first-order transition between two phases of liquid water: LDL and HDL. In this hypothesis, LDA and HDA are simply their corresponding vitreous forms. The transition terminates at a LL critical point. Below this hypothesized *second* critical point (C') the liquid phase separates into two distinct liquid phases: a LDL phase at low pressures and a HDL at high pressure (Fig. 2). Near the hypothesized LL critical point bulk water is a fluctuating mixture of molecules whose local structures resemble the two phases, LDL and HDL. The "critical fluctuations" that are enhanced well above the critical temperature influence the properties of liquid bulk water, thereby leading to the observed anomalies. This theory predicts that the second low-T liquid–liquid critical point is at $T_{C'} \approx 200$K, $P_{C'} \approx 1$ kbar. This approach has been supported by several theoretical studies [26–29].

From a structural point of view, all the proposed scenarios give a key role to the tetrahedral geometry of the local HB interaction pattern. In the liquid state this HB network governs the overall structure and dynamics of water. Further, the LLPT approach focuses on the so-called Widom line, that is, the locus of the maximum correlation length [30,31]. Along the Widom line, the response functions show extremes and finally diverge at the critical point.

Due to the experimental difficulty in exploring the No-Man's Land, the phase diagram shown in Fig. 2 and the physical scenario proposed by the LLPT hypothesis (and in particular the Widom line) until very recently were only hypothesized and not completely proven. The power-law approach, used for many years to explain water singularities, corresponds to the extension of a first-order transition line beyond the critical point. Thus, when experimentally approaching the Widom line, the thermodynamic response functions should behave as though they were going to diverge with critical exponents, but they do not.

A. Selected Experimental and Simulation Results

Many experiments have been performed to test the various hypotheses discussed in the previous section, but there is as yet no widespread agreement on which physical picture, if any, is correct. The connection between liquid and the two amorphous forms predicted by the LLPT hypothesis is difficult to prove experimentally because supercooled water freezes spontaneously below the nucleation temperature T_H, and amorphous ice crystallizes above the crystallization temperature T_X [32,33]. Crystallization makes experimentation on the supercooled liquid state between T_H and T_X almost impossible. However, comparing experimental data on amorphous ice at low temperatures with those of liquid water at higher temperatures allows an indirect discussion of the relationship between the liquid and amorphous states. It is found from neutron diffraction studies [10] and simulations that the structure of liquid water changes toward the LDA structure when the liquid is cooled at low pressures and changes toward the HDA structure when cooled at high pressures, which is consistent with the LLPT hypothesis. Because their entropies are small, the two amorphous states are presently considered to be smoothly connected thermodynamically to the liquid state [34].

In principle, it is possible to investigate experimentally the liquid state in the region between T_H and T_X during the extremely short-time interval before the liquid crystallizes into ice [8,33]. Because high-T liquid bulk water becomes LDA without crystallization when it is cooled rapidly at 1 bar [35], LDA appears directly related to liquid water. A possible connection between liquid bulk water at high pressure and HDA can be seen when ice crystals are melted by increasing the pressure [8]. Other experimental results [33] on the high-pressure ices that might demonstrate a LL first-order transition in the region between T_H and T_X have been obtained.

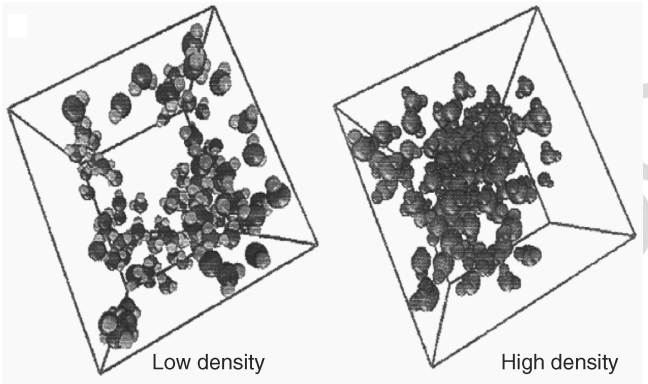

Figure 3. Molecular dynamics snapshots of LDL and HDL, coexisting and separating in liquid water [3].

Water is challenging to simulate because it is a molecular liquid for which there is no precise yet tractable intermolecular potential that has been universally accepted. Nevertheless simulations have some distinct advantages over experiments. Although experiments cannot probe the "No-Man's Land," simulations can probe structure and dynamics well below T_H because nucleation does not occur on the timescale used by computer simulations. Of the three hypotheses above, the LLPT hypothesis is best supported by simulations, some using the ST2 potential, which exaggerates the real properties of bulk water, and others using the SPC/E and TIP4P potentials, which underestimate them [25,36,37]. Recently simulations have begun to appear using the more reliable TIP5P potential [38,39]. The precise location of the LL critical point is difficult to obtain since the continuation of the first-order line is a locus of maximum compressibility.

Further, computer simulations may be used to probe the local structure of water. At low temperatures, many water molecules appear to possess one of two principal local structures, one resembling LDA and the other HDA [25,36,40]. Experimental data can also be interpreted in terms of two distinct local structures [41,42]. Figure 3 is a MD snapshot of LDL and HDL phases coexisting and separating in liquid water. The subset of water molecules in the left panel have a smaller local density than the average, whereas the one reported in the right panel have a larger local density [3].

B. Understanding "Static Heterogeneities"

The systems in which water can be confined are diverse, including the rapidly developing field of artificial "nanofluidic" systems (devices on the order of a

nanometer or less that convey fluids). Confined water is of interest because phenomena that occur at a given set of conditions in bulk water occur under perturbed conditions for confined water [43–45]. For example, the coordinates of the hypothesized LL critical point lie in the experimentally inaccessible No-Man's Land of the bulk water phase diagram, but appear to lie in an accessible region of the phase diagrams of both two-dimensionally and one-dimensionally confined water [46]. Simulations have been carried out to understand the effect of purely geometrical confinement [47,48] and of the interaction with hydrophilic [49] or hydrophobic [50] surfaces. Studying how confinement affects the phase transition properties of supercooled water [48] may also help us clarify the possible presence of a LLPT in water. Recent work on the phase behavior of confined water suggests a sensitive dependence on the interaction with surfaces [50], as the existence of a LLPT appears to be consistent with simulations of water confined between two parallel flat hydrophobic walls. Efforts are being made to extend this work to hydrophilic pores, such as those in Vycor glasses or biological situations, and to hydrophobic hydrogels, systems of current experimental interest [51–53].

C. Potentials with Two Characteristic Length Scales

A critical point appears if the pair potential between two particles of the system exhibits a minimum, and Fig. 4a shows such an idealized system. At high T, the system's kinetic energy is so large that the potential well does not have an effect, and the system is in a single "fluid" (or gas) phase. At $T < T_C$ and $P > P_C$, the fluid is influenced by the minimum in the pair potential such that it can condense into the low specific volume (V) liquid phase. At lower P ($P < P_C$), the system explores the full range of distances, the large V gas phase.

If the potential well has the form shown in Fig. 4a, the attractive potential well of Fig. 4b is now bifurcated into a deeper outer subwell and a more shallow inner subwell. Such a two-minimum potential can give rise to the occurrence at low temperatures of a LL critical point at ($T_{C'}$, $P_{C'}$) [55]. At high T, the system's kinetic energy is so large that the two subwells have no appreciable effect on the thermodynamics and the liquid phase can sample both subwells. However at $T < T_{C'}$ and $P < P_{C'}$, the system must respect the depth of the outer subwell and the liquid phase "condenses" into the outer subwell (the LDL phase). At higher P, it is forced into the shallower inner subwell (the HDL phase).

The above arguments concern the average or "thermodynamic" properties, but can also help us determine the local properties of individual molecules [41]. We take an idealized fluid with a potential of the form of Fig. 4a and suppose that T is, say, 1.2 T_C so that the macroscopic liquid phase has not yet condensed out. Although the system is not entirely in the liquid state, small clusters of molecules begin to coalesce into the potential well, thereby changing their characteristic interparticle

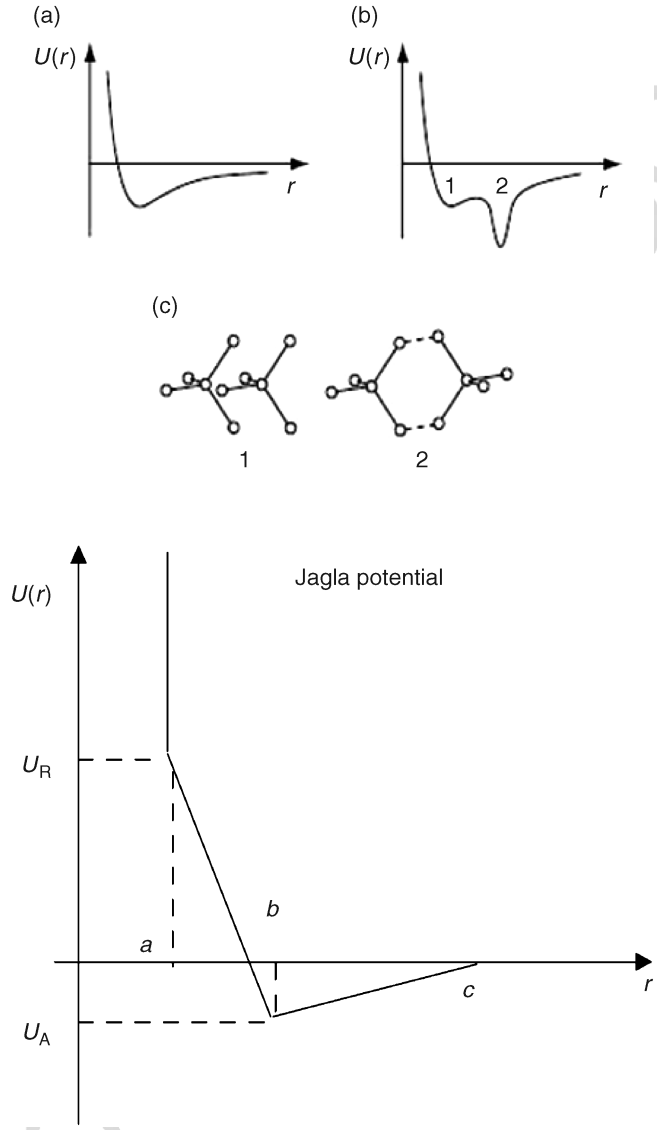

Figure 4. Top: **(a)** Idealized system characterized by a pair interaction potential with a single attractive well. **(b)** Idealized system characterized by a pair interaction potential whose attractive well has two subwells, the outer of which is deeper and narrower. **(c)** Two idealized interaction clusters of water molecules in configurations that may correspond to the two subwells of (b). Bottom: the "two-scale" Jagla ramp potential with attractive and repulsive ramps [54].

spacing (and hence their local V and entropy, S), and the fluid system experiences spatial fluctuations characteristic of the liquid phase even though this phase has not yet condensed out of the fluid at $T = 1.2\ T_C$. δV fluctuations are measured by the $K_T(T)$ and δS fluctuations by the $C_p(T)$, so these two functions should start to increase from the values they would have if there were no potential well at all. As T decreases toward T_C, the magnitude of the fluctuations (and hence of the $K_T(T)$ and the $C_p(T)$) increases monotonically and in fact diverges to infinity as $T \to T_C$. The cross-fluctuations of δV and δS are proportional to the coefficient of thermal expansion (α_p), and this (positive) function should increase without limit as $T \to T_C$.

Consider an idealized fluid with a potential of the form shown in Fig. 4b, and suppose that T is now *below* T_C but is 20% *above* $T_{C'}$, so that the LDL phase has not yet condensed out. The liquid can nonetheless begin to sample the two subwells and clusters of molecules will begin to coalesce in each well, with the result that the liquid will experience spatial fluctuations characteristic of the LDL and HDL phase even though the liquid has not yet phase separated. The δV and δS fluctuations will increase, and the K_T and C_p begin to diverge. When the outer well is narrow, if a cluster of neighboring particles samples the outer well it has a larger V and a smaller S, thus the anticorrelated cross-fluctuations (α_p) are now *negative* and approaching $-\infty$ as T decreases toward $T_{C'}$.

When the value of $T_{C'}$ is lower than the value of T_H, the phase separation discussed above occurs only at temperatures so low that the liquid freezes! In this case, the "hint" of the LL critical point C′ is the presence of these local fluctuations, whose magnitude grows as T decreases, but never diverges if the point C′ is never reached. Thermodynamic functions are observed experimentally to increase if they diverge to ∞ or $-\infty$ but at a temperature below the range of experimental accessibility.

When considering a complex and unknown nonlinear potential between water molecules, the tetrahedrality of water dictates that the outermost well corresponds to the ordered configuration with lower S. Thus, although we do not know the actual form of the intermolecular potential in bulk water, it is not implausible that the same considerations apply as those discussed for the simplified potential shown in Fig. 4b. Indeed, extensive studies of such pair potentials have been carried out recently and the existence of the LL critical point has been demonstrated in such models [27–29,56–58].

More concrete and plausible conclusions are obtained with a bifurcated potential well of the form of Fig. 4b, considering that one can crudely approximate water as a collection of 5-molecule groups called Walrafen pentamers (Fig. 4c) [41]. The interaction strength of two adjacent Walrafen pentamers depends on their relative orientations. The first and the second energy minima of Fig. 4b correspond to the two configurations of adjacent Walrafen pentamers with different mutual orientations (Fig. 4(c)). The two local configurations (1 and 2) in Fig. 4c are

(i) a high-energy, low-V, high-S, nonbonded state (1), or (ii) a low-energy, high-V, low-S, bonded state (2). The difference in their local structure resembles the difference in the local structure between a high-P crystalline ice (such as ice VI or ice VII) and a low-P crystalline ice (such as ice I_h) (Fig. 4(c)).

The region of the P–T plane along the line continuing from the LDL–HDL coexistence line extrapolated to higher T above the second critical point is the locus of points where the LDL, on the low-P side, and the HDL, on the high-P side, are continuously transforming. This is called the Widom line and is defined to be the locus of points where the correlation length is maximum. Near this line, two different kinds of local structures, having either LDL or HDL properties, "coexist." The entropy fluctuations are largest near the Widom line, so here C_p shows a maximum, displaying a λ-like appearance [59]. The increase in C_p resembles the signature of a glass transition as suggested by mode-coupling theory (MCT) [60]. Careful measurements and simulations of static and dynamic correlation functions [61,62] may be useful in determining the exact nature of the apparent singular behavior near 220K.

D. Two Length Scales Potentials: Tractable Models

The above discussion is consistent with the possible existence of two well-defined classes of liquids: simple and water like. The formers interact via spherically symmetric nonsoftened potentials and do not exhibit thermodynamic or dynamic anomalies. One can calculate translational and orientational order parameters (t and q), and project equilibrium state points onto the (t, q) plane thereby generating what is termed the Errington–Debenedetti (ED) order map [24]. In water-like liquids, interactions are orientation dependent; these liquids exhibit dynamic and thermodynamic anomalies, and their ED "order map" is in general two-dimensional but becomes linear (or quasi-linear) when the liquid exhibits structural, dynamic, or thermodynamic anomalies.

Hemmer and Stell [55] showed that in fluids interacting via pairwise-additive, spherically symmetric potentials consisting of a hard core plus an attractive tail, softening of the repulsive core can produce additional phase transitions. This pioneering study elicited a considerable body of work on so-called core-softened potentials that can generate water-like anomalies [58,63–67]. This important finding implies that strong orientational interactions, such as those that exist in water and silica, are not a necessary condition for a liquid to have thermodynamic and dynamic anomalies.

A core-softened potential has been used [55] to explain the isostructural solid–solid critical point present in materials such as Cs and Ce, for which the shape of the effective pair potential obtained from scattering experiments is "core-softened" [2,55,64,65,68]. Analytical work in 1d, 2d, and 3d have suggested a LLPT but not density anomalies [58,65,66,69,70]. The continuous version of the shouldered

attractive potential showed not only the LL critical point but also the density anomaly. The soft-core potential was used to investigate the relationship between the configurational entropy S_{conf} and the diffusion coefficient D. Recent work using the SPC/E potential [70] has suggested that the temperature–density dependence of S_{conf} may correlate with D, and that the maximum of S_{conf} tracks the density maxima line.

Two questions arise naturally from this emerging taxonomy of liquid behavior. First, is structural order in core-softened fluids hard-sphere or water-like? Second, is it possible to seamlessly connect the range of liquid behavior from hard spheres to water like by a simple and common potential by simply changing a physical parameter?

Recently a simple spherically symmetric "hard-core plus ramp" potential was used to address the first question [71]. It was found that this core-softened potential, with two characteristic length scales, not only gives rise to water-like diffusive and density anomalies but also to an ED water-like order map. The anomalies evolution was studied by using the ratio λ of hard-core and soft-core length scales as a control parameter. The calculations revealed a negative thermal expansion coefficient (a static anomaly) and an increase of D upon isothermal compression (a dynamic anomaly) for $0 \leq \lambda < 6/7$. As in bulk water, the regions where these anomalies occur are nested domes in the (T, ρ) or (T, P) planes, with the "thermodynamic anomaly dome" contained within the "dynamic anomaly dome." The ED order map evolves from water-like to hard-sphere like in the range $4/7 \leq \lambda \leq 6/7$. Thus, the range of liquid behavior encompassed by hard spheres ($\lambda = 1$) and water like ($\lambda \sim 4/7$) was traversed by simply varying λ. To establish whether a ratio of competing length scales close to 0.6 is generally associated with water-like anomalies in other core-softened potentials new measurements are needed, for example, using a linear combination of Gaussian [72] potentials of different widths to achieve two characteristic length scales.

In order to better understand liquid polyamorphism [73,74], a systematic study was carried out on the effects of λ, the ratio of characteristic energies on the existence of a LL transition, the positive or negative slope of the line of first-order LL transition in the (P, T) plane, and the relationship, if any [58], between the LL transition and density anomalies. Calculations were performed in parallel for both confined and bulk water, and a spherically symmetric potential with two different length scales called the Jagla potential with both attractive and repulsive parts was used [58,64,65]. The potential is defined as

$$U(r) = \begin{cases} \infty & \text{for} \quad r < a \\ U_A + (U_A - U_R)(r-b)/(b-a) & \text{for} \quad a < r < b \\ U_A(c-r)/(c-b) & \text{for} \quad b < r < c \\ 0 & \text{for} \quad r > c \end{cases}$$

where $U_R = 3.5U_0$ is the repulsive energy, $U_A = -U_0$ is the attractive part, a is the hard core diameter, $b = 1.72a$ is the well minimum, and $c = 3a$ is the cutoff at large distance (see Fig. 4).

Using this "two-scale" potential in molecular dynamics simulations [58,65] has revealed a liquid–liquid phase transition with a positively sloped coexistence line ending at a critical point well above the equilibrium melting line, allowing the study of dynamic behavior in the vicinity of this liquid–liquid critical point. Below the critical point, the dynamics in the more ordered HDL are much slower than the dynamics in the less ordered LDL, thus identifying a dynamic crossover and a Widom line (i.e., the extension of the coexistence line into the one-phase region). In addition, the model has suggested a possible general relation between a liquid–liquid phase transition and the change in dynamics.

E. Understanding "Dynamic Heterogeneities"

Both simulations and experiments are consistent with the possibility that the LL critical point, if it exists at all, lies in the experimentally inaccessible No-Man's Land. If this is the case, at least two reactions are possible:

(i) If something is not experimentally accessible, then it does not deserve discussion.

(ii) If something is not experimentally accessible, but its influence *is* experimentally accessible, then discussion is warranted.

Because accepting option (i) means there is nothing more to discuss, option (ii) has guided most of the research thus far. It has been observed that the effects of a critical point extend a long distance from its actual coordinates. If we confine water, the homogeneous nucleation temperature decreases and we can enter the No-Man's Land and look for the LL critical point. Experiments at MIT and Messina have demonstrated that, for nanopores of 1.5 nm diameter, the No-Man's Land disappears and the liquid state can be supercooled all the way down to the glass temperature. Thus, by studying confined water we can directly test, for the first time, the LLPT hypothesis. Using two independent techniques, neutron scattering and NMR, the MIT and Messina groups found a sharp kink in the dynamic properties (a "dynamic crossover") at the same temperature $T_L \approx 225$K [46,75] for both techniques. The calculations on *bulk* models [54] are not inconsistent with the tentative interpretation that this dynamic crossover is caused by the system passing from the high-temperature high-pressure "HDL" side of the Widom line (where the liquid might display fragile behavior) to the low-temperature low-pressure "LDL" side of the Widom line (where the liquid might display strong behavior). By definition, the Widom line, that is, the line in the pressure-temperature plane where the correlation length has its maximum, arises only if there is a critical point. Hence interpreting the MIT–Messina experiments in terms of a Widom line is of

potential relevance to testing experimentally, in *confined* water, the liquid–liquid critical point hypothesis.

The interpretation of the dynamic crossover could have implications for nanofluidics and perhaps even for natural confined water systems, for example, biological macromolecules.

F. Possible Significance of the Widom Line

This interpretation of the MIT–Messina experiments relies on the Widom line concept, which is still not widely accepted—even though it has been widely known among experimentalists since its introduction in the 1958 Ph.D. thesis of J.M.H. Levelt (now Levelt-Sengers) [31]. By definition, a Widom line arises only from a critical point and, if their experiments can be rationalized by the existence of such a Widom line, the MIT–Messina results are consistent with the existence of a LL critical point in confined water.

In a first-order phase transition, thermodynamic functions by definition discontinuously change as one cools the system along a path crossing the equilibrium coexistence line (Fig. 5a, path β). In a *real* experiment, however, this discontinuous change may not occur at the coexistence line because a substance can remain in a supercooled metastable phase until a limit of stability (a spinodal) is reached [2] (Fig. 5b, path β).

If the system is cooled isobarically along a path above the critical pressure P_C (Fig. 5b, path α), the state functions continuously change from the values characteristic of a high-temperature phase (gas) to those characteristic of a low-temperature phase (liquid). The thermodynamic response functions, which are the derivatives of the state functions with respect to temperature (e.g., C_p), have maxima at temperatures denoted $T_{max}(P)$. Remarkably these maxima are still prominent far above the critical pressure [31], and the values of the response functions at $T_{max}(P)$ (e.g., C_p^{max}) diverge as the critical point is approached. The lines of the maxima for different response functions asymptotically approach one another as the critical point is approached, since all response functions become expressible in terms of the correlation length. This asymptotic line is sometimes called the Widom line, and is often regarded as an extension of the coexistence line into the "one-phase regime."

Suppose the system is cooled at constant pressure P_0. (i) If $P_0 > P_C$ ("path α"), experimentally measured quantities will change dramatically but continuously in the vicinity of the Widom line (with huge fluctuations as measured by, e.g., C_p). (ii) If $P_0 < P_C$ ("path β"), experimentally measured quantities will change discontinuously if the coexistence line is actually seen. However, the coexistence line can be difficult to detect in a pure system due to metastability, and changes will occur only when the spinodal is approached where the gas phase is no longer stable.

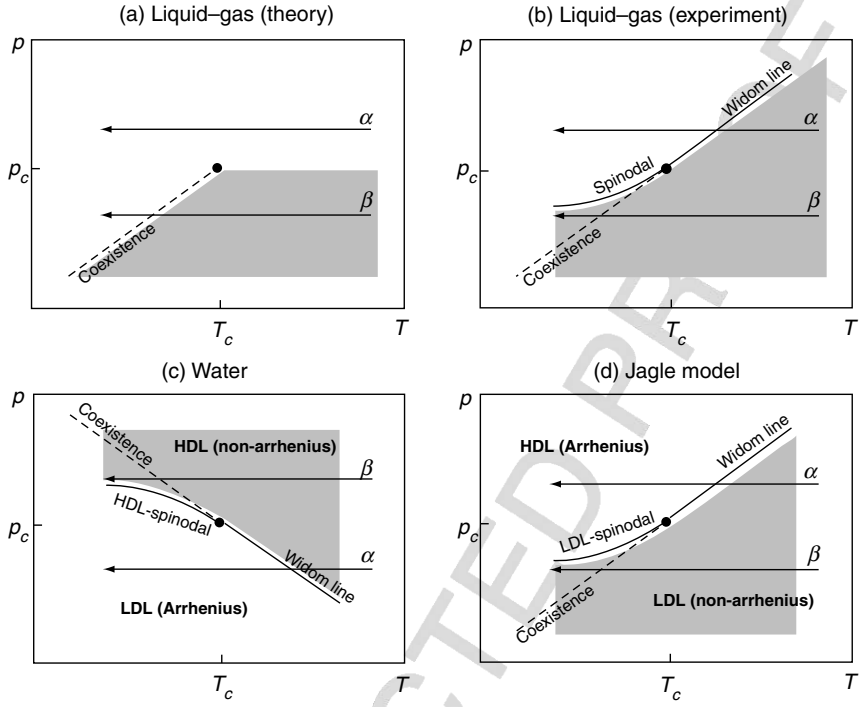

Figure 5. Schematic illustration on the significance of the Widom line [54].

In the case of water, the most important solvent for biological functions [76], a significant change in dynamic properties has been suggested to take place in deeply supercooled states. Unlike other network forming materials [77], water behaves as a fragile liquid in the experimentally accessible window [78]. Based on analogies with other network forming liquids and with the thermodynamic properties of the amorphous forms of water, it has been suggested that, at ambient pressure, liquid water should show a crossover between fragile behavior at high-T to strong behavior at low-T [64,79] in the deep supercooled region of the phase diagram below the homogeneous nucleation line. This region may contain the hypothesized LL critical point [25], the terminal point of a line of a first-order LLPT. Because nucleation can be avoided in confined geometries, dynamic crossovers in confined water were recently studied experimentally [46,48,80]. A dynamic crossover has also been associated with the LLPT in both silicon and silica [81]. The following section tentatively interprets the observed fragility transition in water as occurring when the Widom line emanating from the hypothesized LL critical point is crossed [81] (Fig. 5c and d, path α).

III. METHODS FOR THE CONFINED WATER DYNAMIC CROSSOVER

Using MD simulations [82,83], we studied three models, each of which has a LL critical point. Two (the TIP5P and the ST2) treat water as a multiple-site rigid body that interacts via electrostatic site–site interactions complemented by a Lennard–Jones potential. The third is the spherically symmetric "two-scale" Jagla potential with attractive and repulsive ramps. In all three models the loci of maxima of the relevant response functions, K_T and C_p, which coincide close to the critical point and give rise to the Widom line, were evaluated. The hypothesis that, for all three potentials, a dynamic crossover occurs when the Widom line is crossed, was carefully explored.

For TIP5P, a LL critical point [38,39], from which the Widom line develops, was found. The coexistence curve is negatively sloped, so the Clapeyron equation implies that the high-T phase is HDL and the low-T phase LDL. The diffusion coefficient D was evaluated from the long time limit of the mean squared displacement along isobars. It was found that isobars crossing the Widom line (path α) show a clear crossover (i) from a *non-Arrhenius behavior at high T* [which can be well fitted by a power-law function $D \sim (T - T_{MCT})^{\gamma}$], consistent with the MCT predictions [84], (ii) to an *Arrhenius behavior at low T* [$D \sim \exp(-E_a/T)$]. The crossover between these two functional forms takes place when crossing the Widom line. For paths β, crystallization occurs in TIP5P [38], so the hypothesis that there is no fragility transition cannot be checked at low T. Hence, a related potential, ST2, was considered for which crystallization is absent within the timescale of the simulation [85]. This potential also displays a LL critical point [25,85]. Along paths α a fragility transition may take place, while along paths β the T-dependence of D does not show any sign of crossover to Arrhenius behavior and the fragile behavior is retained down to the lowest studied T. Thus, for paths β, the entire T-dependence can be fit by the MCT power law.

If indeed TIP5P and ST2 water models support the connection between the Widom line and the dynamic fragility transition, it is natural to ask which features of the water molecular potential are responsible for the properties of water, especially because the unusual properties of water are shared by several other liquids whose intermolecular potential has two energy (length) scales such as silicon and silica [81]. Hence, the Jagla potential [64] was also investigated, displaying, without the need to supercool, a LL coexistence line that, unlike water, has a positive slope, implying that the Widom line is now crossed along α paths with $P > P_C$. A crossover in the behavior of $D(T)$ occurs when the Widom line (C_p^{max} line) is crossed, such that at high T, D exhibits an Arrhenius behavior, while at low T it follows a non-Arrhenius behavior, consistent with a power law. Along a β path ($P < P_C$), $D(T)$ appears to follow the Arrhenius behavior over the entire studied T range. Thus, the dynamic crossover coincides with the location of the C_p^{max} line,

extending the conclusion of the TIP5P and ST2 potentials to a general two-scale spherically symmetric potential.

In Ref. [86], the generality of the dynamic crossover in a Hamiltonian model of water that displays a LLPT at low temperatures is investigated. A cell model that reproduces the fluid phase diagram of water and other tetrahedral network-forming liquids was considered (e.g., Ref. [29]). The model is based on the experimental observation that, on decreasing P at constant T or on decreasing T at constant P, (i) water displays an increasing local tetrahedrality [69], (ii) the volume per molecule increases at sufficiently low P or T, and (iii) the O–O–O angular correlation increases [42].

The system is divided into cells $i \in [1, \ldots, N]$ on a regular square lattice, each containing a molecule with volume $v \equiv V/N$, where $V \geq Nv_0$ is the total volume of the system and v_0 is the hard-core volume of one molecule. The cell volume v is a continuous variable that gives the mean distance $r \equiv v^{1/d}$ between molecules in d dimensions. The van der Waals attraction between the molecules is represented by a truncated Lennard–Jones potential with characteristic energy $\epsilon > 0$, and each molecule i has four bond indices $\sigma_{ij} \in [1, \ldots, q]$, corresponding to the nearest-neighbor cells j [86]. When two nearest-neighbor molecules have the facing σ_{ij} and σ_{ji} in the same relative orientation, they decrease the energy by a constant J, with $0 < J < \epsilon$, and form a bond, for example, a (nonbifurcated) hydrogen bond for water, or an ionic bond for SiO_2. When $J < \epsilon$, bonds are formed only in the liquid phase. Bonding and intramolecular (IM) interactions are accounted for by the two Hamiltonian terms

$$\mathcal{H}_{\mathrm{B}} \equiv -J \sum_{\langle i,j \rangle} \delta_{\sigma_{ij}\sigma_{ji}} \quad \text{and} \quad \mathcal{H}_{\mathrm{IM}} \equiv -J_\sigma \sum_i \sum_{(k,\ell)_i} \delta_{\sigma_{ik}\sigma_{i\ell}} \tag{1}$$

where the first sum is over the nearest-neighbor cells, $0 < J < \epsilon$ is the bond energy, $\delta_{a,b} = 1$ if $a = b$ and $\delta_{a,b} = 0$ otherwise, $\sum_{(k,\ell)_i}$ denotes the sum over the IM bond indexes (k, l) of the molecule i, and $J_\sigma > 0$ is the IM interaction energy with $J_\sigma < J$, which models the angular correlation between the bonds on the same molecule. The total energy of the system is the sum of the van der Waals interaction of Eqs. (2) and (3).

Different response functions such as C_p and α_p show maxima, and these maxima increase and seem to diverge as the critical pressure is approached, consistent with the Widom line picture discussed for other water models in the sections above. Moreover, the temperature derivative of the number of hydrogen bonds $\mathrm{d}N_{\mathrm{HB}}/\mathrm{d}T$ displays a maximum in the same region where the other thermodynamic response functions have maxima, suggesting that the fluctuations in the number of hydrogen bonds is at a maximum at the Widom line temperature T_{W}. To further test whether this model system also displays a dynamic crossover as found in the other models of water, the total spin relaxation time of the system as a function of T for different

pressures was studied. For $J_\sigma/\epsilon = 0.05$ (*liquid–liquid phase transition hypothesis*), the crossover occurs at $T_W(P)$ for $P < P_{C'}$. For completeness, the system was also studied in the case of a *singularity-free scenario* corresponding to $J_\sigma = 0$. For $J_\sigma = 0$, the crossover is at $T(C_p^{max})$, the temperature of C_p^{max}.

We then calculated the Arrhenius activation energy $E_a(P)$ from the low-T slope of $\log \tau$ versus $1/T$ and extrapolated the temperature $T_a(P)$ at which τ reaches a fixed macroscopic time $\tau_a \geq \tau_c$, with $T_a(P)$ smaller than the crossover temperature. For $\tau_a = 10^{14}$ Monte Carlo (MC) steps > 100 s, $E_a(P)$ and $T_a(P)$ decrease upon increasing P in both scenarios, providing no distinction between the two interpretations. Instead, there is a dramatic difference in the P-dependence of the quantity $E_a/(k_B T_a)$ in the two scenarios, increasing for the LL critical point and approximately constant for the singularity free.

IV. RECENT EXPERIMENTS ON CONFINED WATER

By confining water in nanosize pores [47,48], it becomes possible to enter into the temperature range inaccessible in bulk water. When water is confined it does not crystallize, and it can be supercooled well below T_H. Porous hydrophilic silica glass, micellar systems or layered vermiculite clay [48] are examples of usable confining nanostructures. Using this technique, the experimentalists were able to study, by means of different experimental techniques like neutron scattering, NMR, and Raman and/or FTIR spectroscopy, the structural and dynamic properties of water in the temperature range $170\text{K} < T < 290\text{K}$. In recent experiments [46,75] on confined water as a function of temperature and pressure, it has been shown that the theoretical LLPT approach is able to describe coherently some of the strange properties of water. Using the neutron scattering technique made it possible to locate evidence of the LL critical point C′ at $T_{C'} = 200\text{K}$ and $P_{C'} = 1.6$ kbar [46] (the Widom line is obtained in the P–T plane—see, e.g., the squares in Fig. 2).

As shown, this result has been qualitatively confirmed by extensive MD simulation analysis [54]. In particular, this MD study used three different models (TIP5P, ST2, and the Jagla potential) to evaluate the loci of maxima of the relevant water response functions (isothermal compressibility and isobaric specific heat), which coincide close to the critical point and give rise to the Widom line. These experiments [46,54,75] are of great interest because their findings have stimulated much of the recent work on water. It has been suggested that a significant change in water dynamics takes place in the deeply supercooled state and that, at ambient pressure, liquid water should show a dynamic crossover from non-Arrhenius at high T to Arrhenius behavior (becoming a strong glass former) at low T [79]. These studies [46,54,75] focus on this fragile-to-strong dynamic crossover (FSC), indicate the connections between the Widom line and the FSC, and connect the crossing of the Widom line to the changes in the HB structure of liquid water. It has been shown

that, upon crossing the Widom line on decreasing T, a breakdown of the Stokes–Einstein relation is observed at $T < T_W(P)$ [87]. Both FSC and BSE take place at T_W and are related to the HDL-to-LDL changes in the dynamic properties and structure of water. Because the LDL phase has been observed in a FTIR experiment [88] it is possible that other new phenomena can occur in water on crossing this line, all of them being related to the changes in the local water structure that take place when the system changes from the "HDL-like" side to the "LDL-like" side. Examples are (i) the systematic changes in the static structure factor $S(q)$ and the corresponding pair correlation function (PCF) $g(r)$, which reveal that, according to the FTIR results [88] for $T < T_W$, the system structure resembles more that of LDL than that of HDL, (ii) the appearance, for $T < T_W$, of a shoulder (Boson peak) in the dynamic structure factor $S(q, \omega)$ at a frequency $\omega \approx 60$ cm^{-1} [89,90], (iii) a rapid increase in the degree of hydrogen bonding for $T < T_W$, (iv) a minimum in the density at low temperature [39,91], and (v) a scaled equation of state near the critical point C′ [92]. We review the FSC and the BSE, using local vibrational modes of the $S(q, \omega)$ to observe the LDL phase, and scattering methods to observe the water density minimum in the supercooled region at $\approx$ 200K. These results are strongly connected to changes in the local structure of water when the system evolves from the HDL to the LDL phase.

To confine water, a micelle template mesoporous silica matrix MCM-41-S with 1D cylindrical tubes arranged in a hexagonal structure was synthesized using the zeolite seed method [46], with hydration levels of $h \simeq 0.5$ (0.5 g H_2O per gram of MCM). As shown by XRD [93], differential scanning calorimetry (DSC) [94], and NMR [95] experiments, this water confining system is one of the most suitable adsorbent models currently available. In particular, the XRD data through the diffracted wave vector, Q_0, of the first sharp water diffraction peak, give the following results: water in MCM-41-S with a pore diameter $\phi = 42$ Å has a sudden freezing at $T \approx 232$K, whereas for $\phi = 24$ Å, it remains in a liquid state down to $\sim$ 160K. Moreover, in the MCM-41-S samples, water freezes with a Q_0 value that is nearly the same as that of the LDA phase ($Q_0^{\text{ice-c}} = 1.71$ Å^{-1}), in contrast to the stable ice–h, usually obtained by freezing bulk water ($Q_0^{\text{ice-h}} = 1.6$ Å^{-1}). In both the samples no Bragg peak, characteristic of crystallization, is observed.

A. Nuclear Magnetic Resonance

Dynamic properties of water confined in fully hydrated MCM-41-S samples with $\phi = 24$, 18, and 14 Å, were studied at ambient pressure and different temperatures by using an NMR spectrometer, operating at 700 MHz ^{1}H resonance frequency. In these NMR experiments, the self-diffusion coefficient of water D, and the maximum intensity $I^{\max}$ of the ^{1}H-NMR spectra—obtained by free-induction decay (FID)—were measured. The explored temperature range was 190–298K. D was

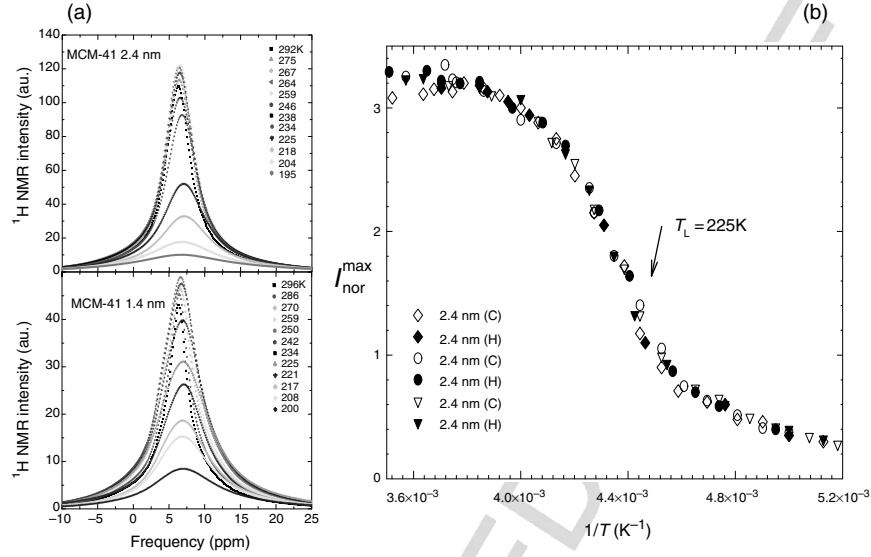

Figure 6. (a) The ^{1}H NMR spectra of water in MCM samples with $\phi = 24$ and 14 Å, upon cooling. (b) The normalized NMR intensities, I^{max}_{Nor} versus $1/T$, for $\phi = 14$, 18, and 24 Å samples [75].

measured with the pulsed gradient spin-echo technique (^{1}H-PGSE) and its thermal behavior will be shown in the next section.

The ^{1}H NMR spectra of water upon cooling in MCM samples with $\phi = 24$ and 14 Å are shown in Fig. 6a. Note that all the reported spectra are characterized by only one resonance peak centered at about 7 ppm. The results differ completely from those obtained from a MCM sample with silanol groups on the internal surface where two resonance contributions are observed. The full width at half-height of these spectra, $\Delta\nu_{1/2} \sim 1/T_2^*$, is the rate of the so-called *apparent* spin–spin relaxation time T_2^* [96]. Note that the maximum intensity of the spectra (I^{max}) decreases and the corresponding linewidth increases upon decreasing T. The crystalline ice phase (characterized by a very large linewidth) is not observed. The NMR signal intensity is directly related to the system equilibrium magnetization, M_0 (or the susceptivity χ_0), which depends linearly on the total number of mobile spins per unit volume, the mean square value of nuclear magnetic moment, and on $1/T$ (the Curie law). Figure 6b shows I^{max}, for $\phi = 14$, 18, and 24 Å samples, upon both cooling and heating, corrected for the Curie effect and normalized to the pore volume, as I^{max}_{Nor} versus $1/T$. Note that the T-behavior of confined water is independent of pore size. Figure 6b clearly shows that there is a steep decrease of I^{max}_{Nor} on decreasing T, at around 225K (T_L). This behavior indicates the location of the dynamic crossover in water. In general, relaxation measured in an NMR

experiment is caused by random fluctuations of the magnetic field located where resonating spins are the result of thermal motion in neighboring spins. In our case, the fluctuating magnetic dipole–dipole interactions between ^{1}H spins are due to the tumbling of molecules under the local caging structure. Hence, the observed behavior of $I_{\mathrm{Nor}}^{\max}$ can be related to the water structure and in particular to its packing density. The probability of a water molecule tumbling is higher in the HDL phase than in the LDL phase. The temperature behavior of $I_{\mathrm{Nor}}^{\max}$ shown in Fig. 6b reflects just such a situation, indicating $T \sim 225$K as the possible crossover temperature between the HDL and the LDL phase.

B. Neutron Scattering

Neutron scattering methods have been used in the past primarily to explore both the structural and dynamic properties of bulk water. One example is a study in which the two phases of the water polymorphism were described, that is, the LDL and the HDL [42]. These experiments were on compressed water in a temperature regime in which the anomalous properties of water are most visible, that is, close to the ice I/ice III triple point ($T = 251$K, $P = 209$ MPa). The OO, OH, and HH partial structure factors and the site–site radial distribution function between distinct atoms were extracted from the diffraction data. If we assume that the structure of water can be represented as a linear combination of the structures of the end points, that is, the HDL and LDL structures, we obtain two values for the densities: $\rho_{\mathrm{HDL}} = 1.20$ g cm^{-3} (0.0402 molecules Å^{-3}) and $\rho_{\mathrm{LDL}} = 0.88$ g cm^{-3} (0.0295 molecules/Å^3). These values are close to the reported densities of high-density and low-density amorphous ice [97].

The neutron methods used to study properties of confined water in the P–T phase diagram include elastic-neutron scattering (ENS), quasi-elastic-neutron scattering (QENS), and inelastic-neutron scattering (INS). These methods allow the study of hydrogen atom dynamics in a number of different confined systems and geometries (e.g., protein hydration water). Because the slowing of water dynamics upon supercooling is exponential, using both a time-of-flight (TOF) and a backscattering spectrometer has been necessary to study water in the region $T = 235$–200K. It is well known that the double differential scattering cross section is proportional to the number of scatterers and the self-dynamic structure factor $S(Q, \omega)$ of the scattered atoms. The self-dynamic structure factor $S(Q, \omega)$ includes the elastic, quasi-elastic, and inelastic scattering contributions. In addition, it can be expressed as a Fourier transform of the self-intermediate scattering function (ISF) of a typical atom $F(Q, t)$, which represents the density–density time correlation function of the tagged atom.

In the case of water, this function relative to the hydrogen atoms, $F_{\mathrm{H}}(Q, t)$, is the quantity of theoretical interest related to the experiment, and it can be calculated in a straightforward way by molecular dynamics simulations. A appropriate

model is the relaxing cage model (RCM) [98] developed to treat supercooled water, and its accuracy has been tested with MD simulations of SPC/E water. Using this model, the water dynamics can be described by means of $F_H(Q,t)$ when considering both the translational (F_T) and the rotational (F_R) motions as $F_H(Q,t) \approx F_T(Q,t)F_R(Q,t)$—contributions that can be separated into short-time and in a long-time parts [98]. The RCM assumes that the short-time translational dynamics of the tagged (or the trapped) water molecule can be regarded as the motion of the center of mass (CM) in an isotropic harmonic potential well caused by the mean field generated by its neighbors. Thus, the short-time part of the translational ISF in the Gaussian approximation can be written in terms of the mean squared deviation of the hydrogen atoms $\langle r^2_{CM}(t)\rangle$. If we consider the translational density of states [60,98] according to the ideal MCT [60] for which the cage relaxation at long time (standard α-relaxation) can be described as a stretched exponential having a structural relaxation time τ_T and a stretch exponent β, the translational ISF valid for the entire time range will be the product of the short-time and long-time parts,

$$F_T(Q,t) \approx F_T^s(Q,t)\exp\left[-(t/\tau_T)^\beta\right] \tag{2}$$

A similar form is obtained for the rotational motion in terms of the Sears exact expansion by means of the lth-order rotational correlation function (RCF), with an expression for $C_1(t)$ in the entire time range given by

$$C_1(t) = C_1^S(t)\exp\left[-(\tau/\tau_R)^{\beta_R}\right] \tag{3}$$

At short times, the orientation of the central water molecule is fixed by the H bonds to its neighbors. It performs oscillations around the HB direction that are nearly harmonic. This dynamic behavior is described by $C_1^S(t)$. At longer times, the bonds break, the cage begins to relax, and the particle can reorient itself, losing its memory of its initial orientation. Thus, the first-order rotational correlation function eventually decays to zero by a stretched exponential relaxation. The RCM model demonstrates that the higher order correlation functions are thus determined from $C_1(t)$[98] and that in the decoupling approximation $F_H(Q,t) = F_T(Q,t)F_R(Q,t)$. The $F_H(Q,t)$ can be written

$$F_H(Q,t) = F_T(Q,t)F_R(Q,t) + F_{con}(Q,t) \tag{4}$$

where $F_{con}(Q,t)$ describes the strength of the coupling between translational and rotational motions as a function of Q and t, as observed by QENS. A detailed analysis shows that the decoupling approximation for the ISF $F_H(Q,t)$ can be used to analyze QENS data from both bulk and confined water. Within this approximation, one only needs to compute $F_T(Q,t)$ and $F_R(Q,t)$ separately. Thus, the RCM model is appropriate for analyzing $F_R(Q,t)$ as well, the essential input

quantity being the translational density of states of the hydrogen atom. Therefore, in confined water QENS experiments one has to take into account only the signal coming from the hydrogen atoms and, denoting the elastic contribution arising from the confining material by p, one can analyze the experimental normalized data,

$$S(Q,\omega) = pR(Q_0,\omega) + (1-p)\mathrm{FT}\{F_\mathrm{H}(Q,t)R(Q_0,t)\} \tag{5}$$

where $F_\mathrm{H}(Q,t) \sim F_\mathrm{T}(Q,t)$, $R(Q_0,\omega)$ is the experimental resolution function, and the symbol FT denotes the Fourier transform from time t to frequency ω. $F_\mathrm{H}(Q,t)$, calculated according to the equations of RCM. Both F_T^s and C_l^S were calculated using the parameters obtained from MD simulations, which are in agreement with experimental results. Because τ_T obeys the power law $\tau_\mathrm{T} = \tau_0(aQ)^{-\gamma}$ [98], the measured spectra, recorded at any T, have been fitted using four parameters τ_0, τ_R, γ, and β, with satisfactory results.

Figure 7 reports the T-dependence of the product $\beta\gamma$, as obtained from the RCM fits. The inset shows the T-behavior of β in the measured temperature range in which both the DCS and HFBS spectra give a value $\beta \approx 0.5$. The product $\beta\gamma$ is the actual exponent of the Q-dependence of the ISF. Note that $\beta\gamma = 2$ for a free diffusion case. The value of $\beta\gamma$ is 1.3 at 325K. It decreases gradually with T until just before $T \approx 225$K, at which point it drops from 0.80 to 0.25 and continues to drop until it approaches zero at 200K. This precipitous drop of $\beta\gamma$ at

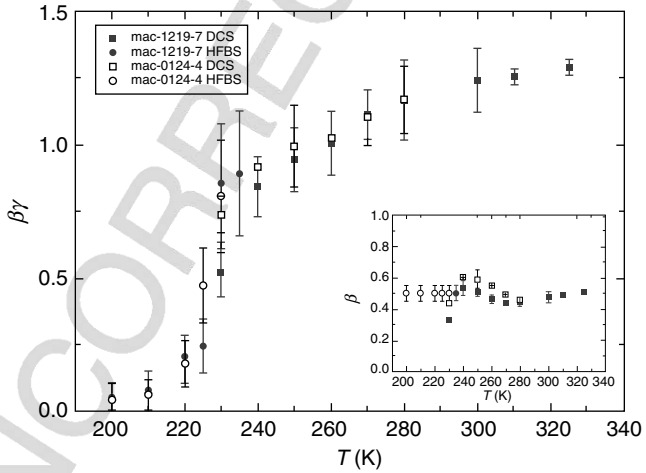

Figure 7. Temperature dependence of $\beta\gamma$, which is the exponent expressing the Q-dependence of the translational ISF for the MCM sample. Note that the figure shows a sharp break at $\approx$ 225K. The inset reports the T-dependence of the exponent β [98].

225K signals a drastic change in the dynamic behavior of water. $\beta \approx 0.5$ clearly indicates that the long-time dynamics of water is nonexponential. Nonexponential behavior is common in supercooled liquids close to the kinetic glass transition. The vanishing value of $\beta\gamma$ indicates the Q-independence of the ISF. It would appear that water is structurally arrested at 200K. It should be noted that the nonexponential and subdiffusive behavior is retained also at room temperature, whereas in MCM with larger pores (> 20Å) a diffusive dynamics is recovered in the limit of high temperature.

V. THE BREAKDOWN OF THE STOKES–EINSTEIN RELATION

Figure 8 is a log-linear plot that shows the temperature variation of the average translational relaxation time $\langle\tau_T\rangle$ for water molecules, obtained at different pressures by the QENS spectra according to the RCM. Figure 8 shows the thermal behavior of $\langle\tau_T\rangle$ for pressures in the range $1 < P < 1600$ bar. Note the transition from a Vogel–Fulcher–Tammann (VFT or "Super Arrhenius") law, $\langle\tau_T\rangle = \tau_0 \exp[BT_0/(T - T_0)]$, where B is a fragility constant and T_0 is the ideal GT temperature, to an Arrhenius law, $\langle\tau_T\rangle = \tau_0 \exp(E_a/k_B T)$. This transition from a VFT to an Arrhenius behavior is the signature of the FSC dynamic transition. The crossover temperature T_L is calculated $1/T_L = 1/T_0 - Bk_B/E_a$.

Figure 2 shows the observed pressure dependence of T_L (squares) and its estimated continuation (dashed line). The T_L line has a negative slope, parallel to the

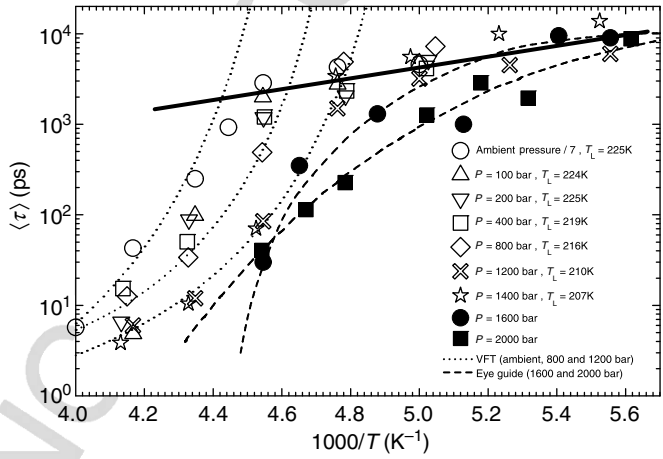

Figure 8. QENS results of hydrated MCM samples ($\phi = 14$ Å) fitted in terms of the RCM analysis. The temperature dependence of $\langle\tau_T\rangle$, at different pressures, are plotted in a log-linear scale versus $1/T$. As it can be seen that a well-defined FSC is observed only for $P < 1600$ bar [46].

T_{md} line, indicating a lower density liquid on the lower T side. This T_L line also closely tracks the T_H line and terminates in the upper end—intersecting the T_H line at 1660 bar and 200K—at which point the character of the dynamic transition changes. According to previous results, confined water remains in a disordered liquid state both above and below the FSC. Furthermore, by considering that the obtained activation energy barrier for initiating the local structure relaxation is $E_A = 5.4$ kcal mol^{-1} for the low-T strong liquid, it is reasonable to conclude that the high-T liquid corresponds to HDL, and the low-T liquid to LDL. Thus, according to the MD simulation study [54], the FSC transition observed at T_L is caused by the crossing of the Widom line and that $T_L \equiv T_W$. The $\langle \tau_T \rangle$ behavior for $P > 1600$ bar is quite different (Fig. 2). At high P, there is no cusp-like behavior characterizing the FSC. In terms of the LLPT and its critical point C′ above the critical temperature $T_{C'}$ and below the critical pressure $P_{C'}$, we are in the one-phase region, whereas when $P > P_{C'}$ there is a two-phase region. Thus, an experiment carried out in this "mixed state" on crossing the LL coexistence line does not produce the large fluctuations observed in the one-phase region, and the thermal behavior of $\langle \tau_T \rangle$ does not show a clear-cut FSC.

Figure 9 shows the ambient pressure values of $\langle \tau_T \rangle$ (QENS data) (Fig. 9a) and the inverse of the self-diffusion coefficient of water $1/D$ measured by NMR (Fig. 9b) for the fully hydrated MCM-41-S samples with pore diameters of 14 Å and 18 Å.

Note that the measured values of D and $\langle \tau_T \rangle$ are independent of the pore size of the samples. This indicates that, because NMR field-gradient measurements have a length scale larger than the pore size, they are insensitive to system geometry. In both figures the solid line denotes the data fit to the VFT law $1/D = 1/D_0 \exp[BT_0/(T - T_0)]$ and the dotted line denotes the fit to the Arrhenius law. From the NMR data we find that $1/D_0 = 2.4 \times 10^7$(s m^{-2}), $B = 1.775$, $T_0 = 187$K, $E_A = 3.98$ kcal mol^{-1} and $T_L = 224.5$K. From the $\langle \tau_T \rangle$ data at ambient pressure, the corresponding values are $T_0 = 200$K, $E_A = 5.4$ kcal mol^{-1}, and $T_L = 225.8$K. The agreement between NMR and QENS results, and the two relevant quantities E_A and T_L in particular, is thus satisfactory. Interpreting the FSC transition as a variant of the structural arrest transition (as predicted by the ideal MCT) was the essence of the QENS study of the structural relaxation time and of the MD study of the self-diffusion coefficient [46,54]. The NMR results presented above thus constitute, by means of a direct measurement of the self-diffusion coefficient of supercooled water, an independent confirmation of the existence of FSC in water.

We now focus on the Stokes–Einstein relation, which relates the self-diffusion coefficient D, viscosity η, and temperature T as $D \propto T/\eta$ and which is known to be accurate for normal- and high-temperature liquids. Since $\langle \tau_T \rangle$ is proportional to the viscosity, the relationship between D and $\langle \tau_T \rangle$ is examined in the inset of Fig. 10, which shows quantity $D\langle \tau_T \rangle / T$ as a function of T.

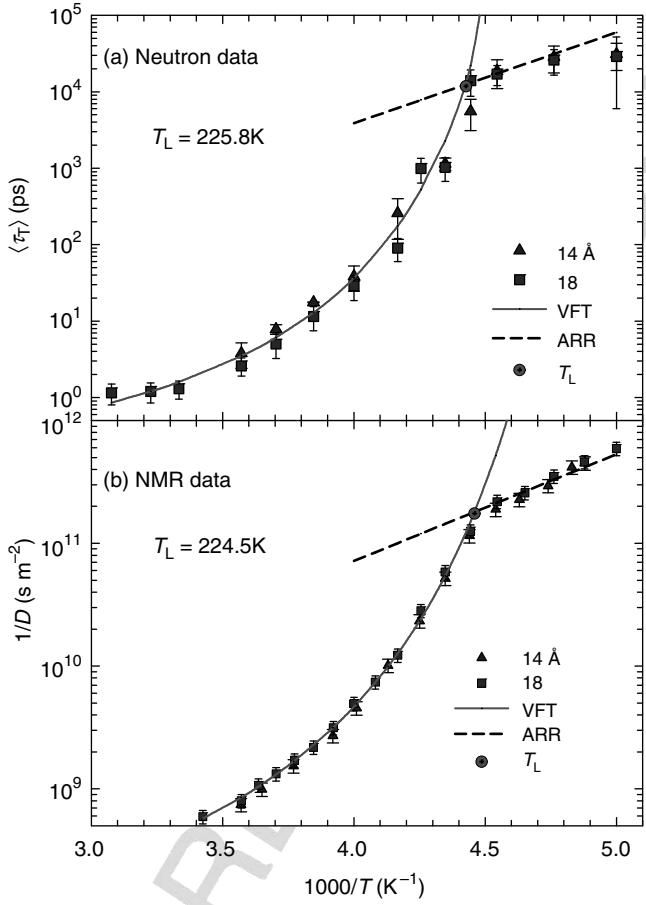

Figure 9. The ambient pressure values of the $\langle\tau_T\rangle$ (a—QENS) and of the $1/D$ (b—NMR) as a function of $1/T$ in fully hydrated MCM-41-S.

The experimental data yields values $\phi = 14\,\text{Å}$ (triangles) and $\phi = 18\,\text{Å}$ (squares), and the dotted line represents the same quantity obtained using the corresponding fitting values reported in Fig. 9a and b. The T-dependence of $D\langle\tau_T\rangle/T$ indicates that this quantity is in the supercooled region inconsistent with the SE law, and signals marked decoupling between these two transport parameters on decreasing T. In recent studies on supercooled liquids, it has been reported that the SE law breaks down as the GT is approached. The self-diffusion coefficient shows an enhancement that differs in orders of magnitude from that expected from SE [99].

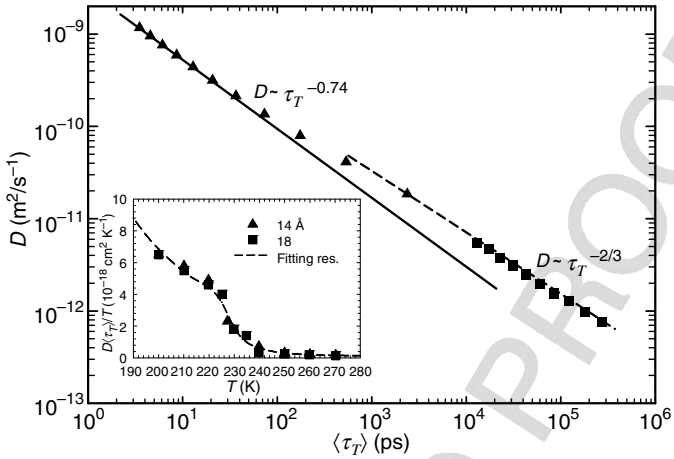

Figure 10. The breakdown of the Stokes–Einstein relation, $D\langle\tau_{\mathrm{T}}\rangle/T$ versus T (inset). Scaling representation of the BSE in a log–log scale of D versus $\langle\tau_{\mathrm{T}}\rangle$ [87].

These decouplings of the transport coefficients, observed as a SE violation, have been attributed to the occurrence of dynamic heterogeneities in structural glass formers [99,100]. Thus, in supercooled liquids there exist regions of varying dynamics, that is, fluctuations that dominate their transport properties near the GT.

The observed breakdown of the Stokes–Einstein relation can be described using scaling concepts, for example, the law $D \sim \tau^{-\xi}$, where $\xi = \alpha(T)/\beta(T)$ with α and β being T-dependent scaling exponents of D and τ, respectively. It has been shown that for tris-naphthylbenzene (a fragile glass former) $\xi = 0.77$, whereas a MD simulation of Lennard–Jones binary mixture has given $\xi = 0.75$ [101]. Figure 10 shows the D versus $\langle\tau_{\mathrm{T}}\rangle$ plot in a log–log scale. The triangles represent data corresponding to temperatures above T_{L} where water behaves as a fragile glass former, and squares pertain to the strong Arrhenius region. Note that the data clearly show two different scaling behaviors above and below the FSC, in particular $\xi \simeq 0.74$ on the fragile side (solid line) and $\sim 2/3$ on the strong side (dashed line).

VI. THE LDL PHASE AND THE WATER DENSITY MINIMUM

FTIR absorption measurements were performed at ambient pressure in the HOH bending and O–H stretching (OHS) vibrational spectral regions in the same samples as in the QENS and NMR experiments. The obtained spectra are reported in Fig. 11. Note that the HOH bending spectra have a Gaussian-like form quite different from the nearly flat form typical of polycrystalline ice, revealing that confined water remains in its liquid state across the entire studied T-range (Fig. 11b).

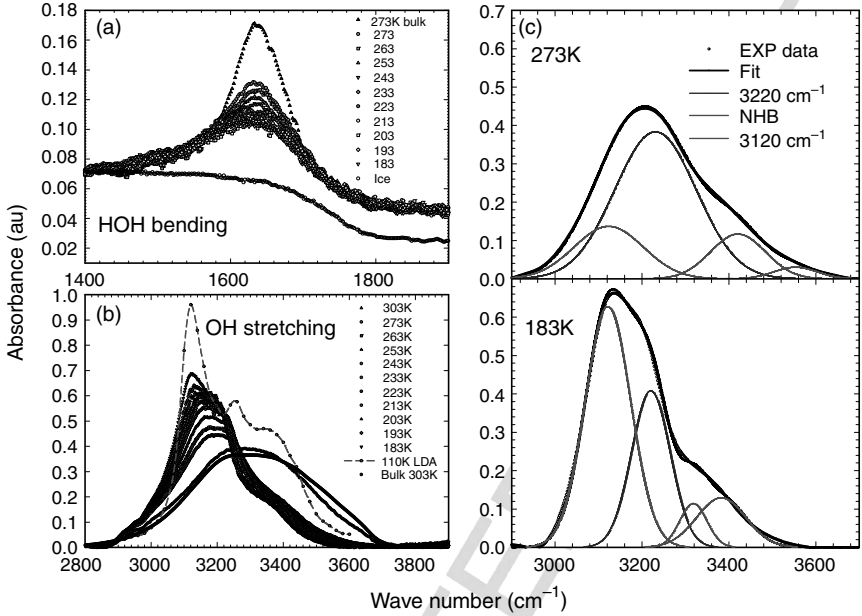

Figure 11. **(a)** The HOH bending and **(b)** the O–H stretching vibrational spectra of MCM confined water at the different temperatures [88]. **(c)** Examples of the spectral fitting results.

Because water is characterized by the presence of two coexisting main HB structural phases involving hydrogen-bonded (HB) and nonhydrogen-bonded (NHB) molecules, it is customary to analyze OHS spectra by considering two general classes of O–H oscillators [42,46,102–104]. These classes encompass broad Gaussian components, each referring to structures that involve a range of bond angles and distances distributed around the component peak position. From the spectral deconvolution we see that the corresponding full widths at half maximum (FWHM) and intensities (integrated areas) change and that the wave numbers fluctuate within the experimental error (± 20 cm^{-1})[103,104].

The OHS spectra of water, as measured by Raman scattering and Infrared absorption from the LDA phase to nearly the first critical point of water, have been described by the following Gaussian component peak positions (wave numbers): (I) 3120 cm^{-1}, (II) 3220 cm^{-1}, (III) 3400 cm^{-1}, (IV) 3540 cm^{-1}, and (V) 3620 cm^{-1}. All have been unambiguously classified as HB, NHB, or OHS oscillators. The situation may be summarized as follows (see, e.g., Fig. 11c):

(a) Component I dominates the intensity of the LDA phase [105] and represents the OHS contribution of molecules forming the "random tetrahedral network" (RTN).

(b) Components II and III have been associated with water molecules having an average degree of connectivity larger than that of monomers, but lower than that involved in the HB networks. Thus, they represent partial HB (PHB) molecules [103,104].

(c) Because components IV and V are the only ones present in the Raman and IR spectra of bulk water in the T region of the first critical point (630K $<$ T $<$ 647K), they arise from NHB monomeric water (or to molecules poorly connected to their environment) [103].

The integrated intensities of PHB and NHB water show an opposite temperature behavior for $T > 300$K. Although the intensities of NHB increase with increasing T, those of PHB decrease. The classification of these contributions reflects that used in the percolation hypothesis for water (f_i species of water, with i indicating the number of bonds) [21]. Thus, HB component I is f_4, NHB components IV and V are f_0, and PHB components II and III are f_1, f_2, and f_3. According to water polymorphism, the HDL phase is represented by both the NHB and PHB components.

Returning to the FTIR measurements on confined water, the proof that OHS spectral component (I) 3120 cm^{-1} represents the LDL liquid phase is obtained when we consider the temperature behavior of its FWHM measured in the LDA phase [105] and measured in MCM confined water [88]. Figure 12 (inset) shows such a quantity versus T in the interval $30K < T <$ 290K. A data continuity from the liquid to the LDA region is evident from the unique analytical curve that indicates a direct link between the contribution (I) of the OHS spectrum and the LDL water phase, and the striking correspondence between LDA and LDL.

We next consider the scattering theory that states that the integrated intensity of the measured spectra $I(Q, \omega)$ is directly proportional to the number of scatterers N. Namely, $I(Q, \omega) \propto (N/V)S(Q, \omega)$. Figure 12 shows the fractional relative populations of the LDL W_{LDL} (diamonds) and the PHB (triangles) and NHB (circles) of the HDL, W_{HDL}, water phases, calculated as the ratio of the component integrated area to the total OHS area for the interval 30 K $< T <$ 373K. These populations are defined as $W_i = N_i/N$, where N_i and N are the number of the particles of the phase i and the total number of scattering particles, respectively. The data are collected from three different experiments. For the 30–130K temperature region, the data are obtained from an analysis of OHS Raman of LDA spectra [105]. For the 183 K $< T <$ 303K temperature region the data are obtained on supercooled confined water [88], and for the 253 K $< T <$ 373K temperature region the Raman data of bulk water [103,104] were analyzed. Note that the behavior of all three species is continuous across the different T ranges even though different data sets were used. This is of relevant, especially for component (I), because, in terms of the corresponding FWHM, it confirms the observation that it is in the LDL liquid phase. Note that the NHB and PHB contributions are present at all temperatures,

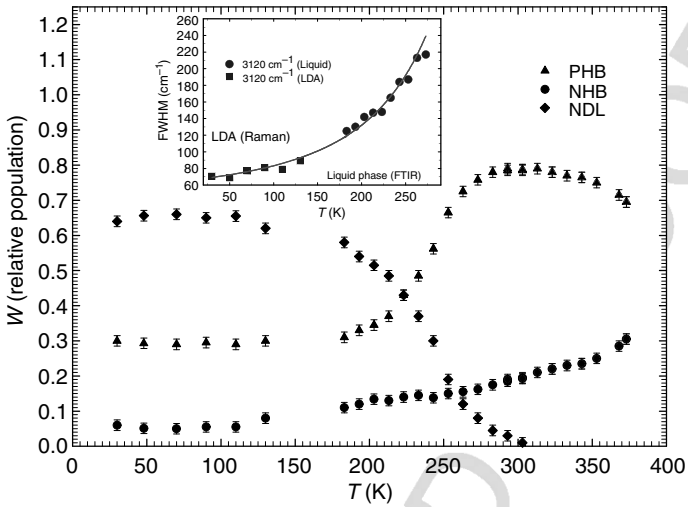

Figure 12. The FWHM values of the OH stretching spectral component I (3120 cm^{-1}) versus T, measured in confined water and in the LDA phase [88,105] (inset). T-dependence of the fractioned relative populations of the LDL, W_{LDL} (diamonds), and of the HDL, W_{HDL} (triangles and circles) water phases [106].

but that the LDL phase exists only when $T \lesssim 303$K. The LDA phase is dominated by LDL, but in the stable liquid phase when $T > 303$K only the HDL is present. The PHB population has a maximum at ≈ 303K, decreases on decreasing T in the entire supercooled region, crosses LDL at about 225K, and finally becomes stable ($W \sim 0.29$) in the LDA phase.

These results show that the HB random tetrahedral network is formed inside the metastable supercooled regime. Note that NHB and PHB are also present in the LDA phase, indicating that the dynamic behavior of LDA is not completely frozen even at $T = 30$K [107].

Finally, the results reported in Fig. 12 have been used to obtain the H_2O density and, by using optical methods, to explore the possibility of a minimum in this quantity. Very recently, using neutron scattering, the existence of a density minimum in the supercooled phase has been observed in confined D_2O at $T_{\mathrm{min}} = 210 \pm 5$K [91]. The idea of a minimum located approximately 70K below density maximum temperature T_{md} has also been suggested by MD simulation studies [39] in which both the TIP5P-E and the ST2 potential models for water have been used [39,85]. This possibility can also be inferred from simple arguments. After the maximum, the density of bulk water decreases rapidly with decreasing T before T_{H}, whereas ice I_h has a smaller density than that of liquid water and, contrary to the behavior of supercooled bulk water, has a normal positive expansivity, that is, ρ increases

as T decreases. The same behavior is observed for LDA at its highest T. From a structural point of view, ice I_h represents the limiting case of a perfectly ordered tetrahedral network of HB, whereas LDA, which forms from deeply supercooled water, has a structure that very closely approaches that of a RTN. Thus, ice I_h sets a lower bound for the density that supercooled water could in principle attain. Hence, if the structure of deeply supercooled water approaches that of a RTN, and if nucleation can be avoided, it is then possible that a density minimum could occur in the deeply supercooled liquid.

Since only water contributes to the reported OHS spectra, its density can be obtained only from the respective densities of its LDL and HDL phases. MD simulations [2], and neutron scattering [42] give values of the corresponding densities: $\rho_{HDL} \approx 1.2 \text{g cm}^{-3}$ and $\rho_{LDL} \approx 0.88 \text{ g cm}^{-3}$, and LDA was experimentally measured [108] as $\rho_{LDA} \approx 0.94 \text{ g cm}^{-3}$. Since the LDL phase exists only when $T < 303$K, HDL water is only given for $T > 303$K by the remaining spectral contributions classified as NHB and PHB.

Water density was calculated from the fractionated populations W_{LDL} and W_{HDL} and their individual local densities ρ_{LDL} and ρ_{HDL}. The W quantities are T-dependent in all the studied liquid regimes and the individual densities may in principle change with temperature. This can be verified by considering the region $T > 303$K, in which only the PHB and NHB species contribute to the OHS spectra [103,104] and ρ_{PHB} and ρ_{PNB} can be obtained from the bulk water density as $\rho_{H_2O} = \rho_{PHB} W_{PHB} + \rho_{NHB} W_{NHB}$, which are the well-known $\rho_{H_2O}(T)$ values for $239\text{K} < T < 423\text{K}$ [5]. Taking into consideration all the W_{PHB} and W_{NHB} data measured in that T interval, we find that $\rho_{PHB} \simeq 1.10 \pm 0.02 \text{g cm}^{-3}$ and $\rho_{NHB} \simeq 0.59 \pm 0.02 \text{g cm}^{-3}$. These values are T-independent within experimental error. This is not surprising since the data on the proton magnetic resonance chemical shift of liquid water in the range $273\text{K} < T < 363K$ (which reflects the local structure of the entire system) reported in the literature does not exhibit any singularity or discontinuity [109]. From this we find that (a) in the considered T range, ρ depends on T only through W, and (b) $\rho_{NHB} \simeq 0.59 \pm 0.02 \text{g cm}^{-3}$, according to Kell's representation [5] of bulk water density as a function of T, corresponds to the density value of H_2O at $T \sim 625$K. This value is smaller than that used in a neutron scattering experiment in the supercritical region (0.66g cm^{-3} for $T = 673$K, at a pressure of 800 bar), where no distinct HB peaks are observable in the O–H radial distribution function g_{OH} [42]. Thus, the value of ρ_{NHB} reasonably represents that of NHB water, which dominates vibrational spectra in the region above the critical temperature (C). In addition, $\rho_{PHB} \simeq 1.10 \pm 0.02 \text{ g cm}^{-3}$ is comparable to the value proposed for HDL water [42]. The contribution of HDL to the total H_2O density, Δ_{HDL}, can thus be obtained throughout the explored T range ($30\text{K} < T < 373\text{K}$) by extending the calculation for ρ_{NHB} and ρ_{PHB} to the lowest temperatures. In a similar way, we calculate the density value of the ρ_{LDL} contribution of that phase, Δ_{LDL}, to the total ρ_{H_2O}. Here, the H_2O

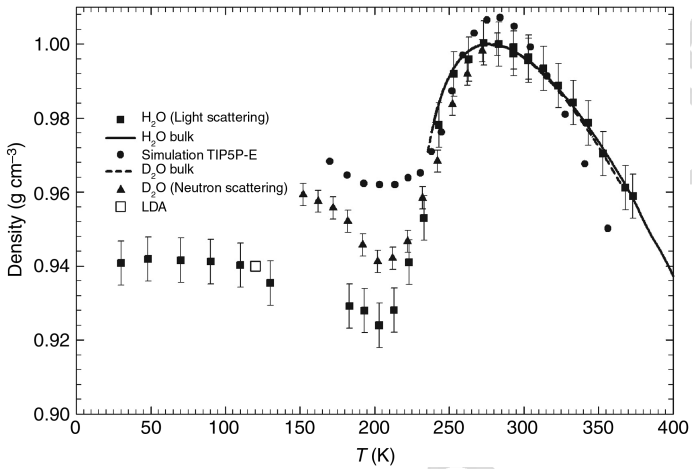

Figure 13. The measured $\rho_{H_2O}(T)$ versus T (squares, [106]); the solid and dot lines refer to bulk densities of H_2O and D_2O, respectively [5]. Triangles represent the $\rho_{D_2O}(T)$ measured by means of neutron scattering [46]. Dots are the bulk density MD values [39] and the open squares are the density of the LDA water at $T = 120$K [108].

density values at temperatures near T_{md} [5] have been considered, and a value $\rho_{LDL} = 0.87 \pm 0.02$g cm^{-3} [106] obtained that closely matches that proposed by neutron diffraction data analysis for LDL water [42]. Thus, ρ_{H_2O} has been calculated to be $\rho_{H_2O} = \Delta_{HDL} + \Delta_{LDL}$ for the temperature interval 30K $< T <$ 370K. Figure 13 shows the plot of water density versus T. For comparison, the values measured in bulk water in the range 239K $< T <$ 423K are also shown [5].

Note that there is good agreement between these "optically measured" density data and the literature data for ρ_{H_2O} in the supercooled regime (where, contrary to the range 273–373K, data were not used to extract the values of ρ_{NHB}, ρ_{PHB}, and ρ_{LDL}). Two findings are remarkable: the minimum at 203 ± 5K and the value of $\rho = 0.940 \pm 0.003$g cm^{-3} in the LDA phase, approximately the same as that measured in LDA ice at $T = 120$K [108]. Looking carefully at the data in the region of deep supercooling (near 250K), we see that the data for confined water are slightly lower than those for bulk water. This may be due to the nanotube confinement, but the difference is not sufficiently relevant to affect the overall result. Figure 13 shows the $\rho_{D_2O}(T)$ data obtained by neutron measurements [46] and the results of the quoted MD simulation of H_2O with the TIP5P-E potential. The ρ_{D_2O} data have been scaled over the ρ_{H_2O} data by taking into account the T shift of the corresponding maxima (about 7K) [39] and the absolute value of the $\rho^{max}_{D_2O}$. Note that there is a good agreement in the overall thermal behavior between $\rho_{D_2O}(T)$ and $\rho_{H_2O}(T)$ data, the only difference being that $\rho_{H_2O}(T)$ includes the densities

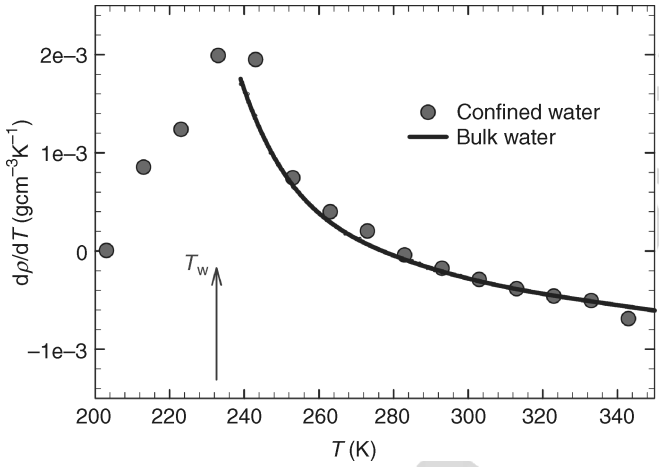

Figure 14. The density derivative $(\partial\rho/\partial T)_p$. The arrow indicates the Widom temperature T_W. $(\partial\rho/\partial T)_p$, related with the cross-correlation between the entropy and volume fluctuations, is proportional to the thermal expansion coefficient [106].

within the LDA phase. There is a marked difference between the experimental and the MD simulation water densities, but it is possible that, with the use of another potential, MD simulation might give results more reliable than those from experiment.

In addition to the density minimum, we can estimate the derivative of the density with respect to temperature $(\partial\rho/\partial T)_p$ and get important experimental results (Fig. 14). Note that this quantity is proportional to the thermal expansion coefficient and has a maximum at the inflection point between the maximum and the minimum at $\rho_{H_2O}(T)$, where the temperature T_L corresponding to the Widom line crossing point at ambient pressure is located. Different phenomena have been correlated with the existence of the Widom line, for example, the SEV, the sharp change and the maximum in the T derivative of the mean squared displacement, and the number of hydrogen bonds per molecule. As mentioned above, the SEV is due to the onset of dynamic heterogeneities with a typical length scale of a few water molecules [110]. The maximum in $(\partial\rho/\partial T)_p$ is thus not influenced by confinement effects. This argument is supported when the same quantity is obtained from the density data of pure supercooled bulk water [5] reported in the same figure as a continuous line. Here, the T-behavior of water density in the supercooled regime has been described as driven mainly by the LDL phase. Thus, $(\partial\rho/\partial T)_p$ reflects the T change of the local tetrahedral order. Note that, from a thermodynamic point of view, the maximum in $(\partial\rho/\partial T)_p$ occurs at the same temperature as the Widom line: the temperature T_L is the locus of the correlation length maximum, whereas

the density derivative is related to the cross-correlation between the entropy and volume fluctuations.

VII. SPECIFIC HEAT AND THE GLASS TRANSITION

The glass transition is one of the most studied condensed matter property. Understanding glass formation is not straightforward, because the existence of a true glass state, distinct from a liquid or a solid, remains elusive. A common interpretation of glasses is that they are liquids that have become too viscous to flow: why does the viscosity of glass-forming liquids increase so dramatically when approaching the glass transition? This phenomenon is also described as "molecular jamming" or dynamic arrest—the molecular degrees of freedom in the system are frozen. Despite decades of research, a clear explanation of this phenomenon, common to materials as diverse as molecular glasses, polymers, granular matter, and colloids, is still lacking. The puzzle is that the static structure factor of a glass is indistinguishable from that of the corresponding liquid, with no sign of increasing correlation length scales accompanying the transition. Theoretical approaches instead reveal the existence of collective phenomena with a growing dynamic length scale [111,112] associated with dynamic heterogeneities [99]. As the GT is approached, the dynamics of the system become sluggish, that is, for flow to continue, increasingly larger regions of the material must move simultaneously. The glass transition temperature T_g is a kind of "critical temperature" [60] and appears to be the separation point between two different statistical regions. In the first, above T_g, the system is a true ergodic liquid. In the second, below T_g, it becomes nonergodic (the system needs extremely long times to explore the phase space). Thus in both the liquid region and the metastable supercooled region the system is in thermal equilibrium, but in the glassy phase it is not. The behavior of this system is scientifically interesting, not only as it approaches T_g, but also as it enters the glass phase (e.g., the aging phenomenon at temperatures below T_g).

In the glassy state, molecules oscillate in a potential energy minimum and the probability that they will jump to a new position at some distance is increasingly small. As the temperature of the glass is increased, this probability increases. When the temperature becomes sufficiently high that Brownian diffusion becomes observable on a laboratory timescale, the glass becomes a liquid. In the liquid state, molecules also oscillate around an equilibrium configuration. Thus, a liquid in which Brownian diffusion occurs also has a solid-like rigidity that is numerically defined by its frequency-dependent shear modulus (viscoelasticity). The relation of the dynamics to the thermal energy and the entropy changes, the constant pressure specific heat $C_p(T)$ and its changes as the "observable" quantity, are of primary significance in the study of the vitrification processes. This dynamic process has been explained using a number of different approaches [113]. One of these involves

observing how a liquid's thermodynamic state point fluctuates in a potential energy landscape [114], that is, describing how the energy of a system changes with the geometry of molecular arrangement, particularly with reference to structural relaxation and viscosity.

It is commonly accepted that vibrational motions are the primary influence on the C_p and the entropy in the glass phase, but that in the liquid phase there are two components: (i) a vibrational component caused by a change in the force constants and frequency with changing T, and (ii) a configurational component caused by a change in the number of arrangements with changing T that the structure of liquid explores [115]. Both contributions change on cooling until the supercooled liquid vitrifies. Thus, C_p of the glass has mostly a vibrational contribution $C_{p,\mathrm{vib}}$. On heating through its softening temperature T_g, this C_p begins to gain the configurational contribution in a t- and T-dependent manner, reaching the full value in the ultraviscous state. Both the vibrational and configurational parts of an equilibrium ultraviscous state's C_p and entropy vary with T. Figure 15 shows the glycerol C_p measured in a freezing–heating cycle by using a specially designed calorimeter [115]. The glycerol T_g is $\approx$ 190K (i.e., the C_p maximum temperature just before the jump from the liquid to the arrested glass phase) and the configurational contribution approximate the difference between the C_p values above and below the jump.

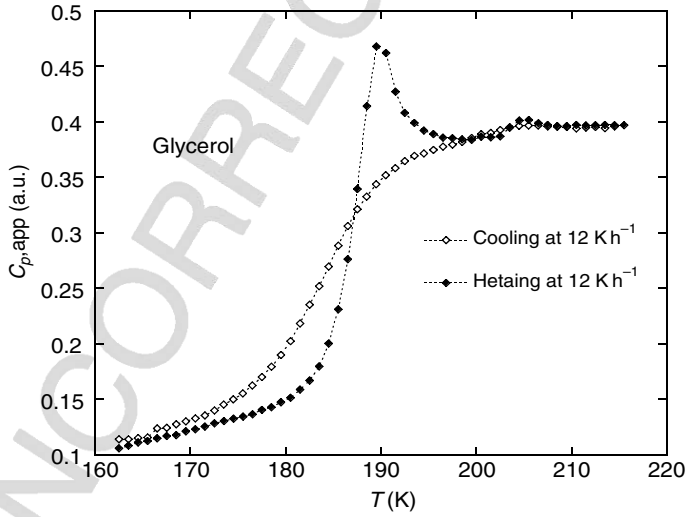

Figure 15. The specific heat measured in glycerol. The maximum gives a clear indication of the onset of the glass transition.

In order to understand the nature and the underlying physics of the glass phase it is important to understand how a supercooled liquid goes toward equilibrium. The role played by the potential energy landscape in system equilibrium dynamics has been given much study. The trajectory of the representative point in the $3N$ configuration space can be mapped into a sequence of locally stable points (the so-called inherent structures, IS [116]), which are the local minima of the total potential energy U. We can associate an IS by the steepest descent path in the U surface to each instantaneous configuration during the dynamic evolution of the system. The IS properties have been found to be very useful in clarifying many features of the dynamics and the thermodynamics of supercooled liquids in both equilibrium and out of equilibrium [117]. Thus, a detailed topological analysis of the potential energy landscape, including all stationary points of U (e.g., minima and saddles) can better represent the system when it is in equilibrium.

A. Specific Heat Measurements in Glass Forming Systems

The approach of the GT can be seen in the strong changes in the thermodynamic response functions, that is, such transport parameters as viscosity (η), the self-diffusion constant (D_s), the ultrasonics, relaxation time (τ) and, in particular, dielectric relaxation time. The response function relaxation times of the liquid increase rapidly as the GT is approached from above. This description takes into account dynamic arrest and characterizes many different systems, that is, not only molecular liquids but also such so-called "complex liquids" as disordered magnets, dipolar glasses, polymers, colloid glasses, and granular materials [118]. In addition, the thermodynamic and dynamic signatures are strongly related. As the τ (or η) of the liquid increases, it takes an ever-increasing amount of time for the thermodynamic quantity to attain its equilibrium value. Thus, at T_g and below T_g the time the system requires to reach equilibration approaches infinity. Consequently τ diverges and the physics of the system becomes increasingly nonlinear.

Under these conditions, studying quantities such as C_p becomes problematic because their significance changes at an T interval near T_g, at which point the system falls out of equilibrium, and we are then faced with the problem of how to interpret a quantity such as C_p in a nonequilibrium state. How a measurement is performed affects the measured values. Thus, if we want to study well-defined equilibrium quantities in the liquid state, and still learn something about the GT, then we must study their dynamic behaviors. Note that in this situation these measurements are not in the linear-response regime (i.e., under nonequilibrium and nonlinear conditions).

Apart from conventional experiments on C_p, we can use a technique appropriate to this complex situation that allows us to measure a sample response to a small perturbation from equilibrium. The traditional way of measuring specific heat involves cooling or heating the sample at a constant rate. But the temperature at

which C_p changes abruptly, signaling the equilibrium-to-nonequilibrium crossover T_g (or vice versa), is strongly dependent on the experimental heating or cooling rate (e.g., when the system is cooled slowly, T_g is lower because the system has more time to equilibrate at each temperature).

"Specific heat spectroscopy" [119] is useful in this regard. Using this tool, we measure the frequency (ω) dependence of C_p, and evaluate the enthalpy (H) derivative $\partial H/\partial T$, and the real and imaginary part of the specific heat, C_p' and C_p'', respectively. In this way, we can show that the relaxation properties of the GT are in the equilibrium state. Only by working in a large frequency range (five decades) it is possible to probe the linear response of a supercooled liquid to a small perturbation from equilibrium and to obtain, by means of calorimetry, thermodynamic information on the zero frequency (by extrapolating from the data obtained).

In a manner similar to the dielectric constant, frequency-dependent $C_p(\omega)$ is defined as a dynamic susceptibility. Under equilibrium conditions, the heat that the system can adsorb from its surroundings during a ΔT change is $q = H = C_p \Delta T$, that is, the change in enthalpy per volume H. If the system contains $\Phi(t)$ relaxing degrees of freedom after a T change, $H = H(t)$. For a time-dependent T variation, $\Delta T(t)$ in a time interval $0 < t' < t$ is

$$q(t) = \int_0^t dt' \{C_{p\infty} + (C_{p0} - C_{p\infty})[1 - \Phi(t - t')]\} \partial T(t')/\partial t' \tag{6}$$

C_{p0} is the equilibrium specific heat and $C_{p\infty}$ includes the faster ones. When $T(t)$ stays close a certain value, C_{p0} and $C_{p\infty}$ will be constant. As in linear susceptibility, C_p can be measured in both the t and ω domains, hence the integration and the Fourier transform of previous equation gives

$$q(t) = C_p(\omega) T(\omega) \quad \text{with} \quad C_p(\omega) = C_{p\infty} + (C_{p0} - C_{p\infty}) \int_0^\infty -\partial \Phi(t)/\partial t \mathrm{e}^{i\omega t} \mathrm{d}t. \tag{7}$$

The static specific heat is then $C_p(\omega = 0) = C_{p0}$, and $C_p(\omega)$ is a complex susceptibility that obeys the Kramers–Kronig relation in both its real and imaginary parts, and that can be related to an equilibrium correlation function. The static specific heat is related to δS at constant P. These are proportional to the enthalpy fluctuations $\delta H(t) = H(t) - \overline{H}$, hence $C_p = V/k_B T^2 \langle \delta H(t)^2 \rangle$, where $\overline{H}$ is the $H(t)$ average. Under ergodic conditions, the angular bracket represents an ensemble or a time average. The fluctuation–dissipation theorem generalizes this result and gives a dynamic susceptibility. When the slow and fast modes are explicitly included in the relaxing function, $\Phi(t) = \langle \delta H(t) \delta H(0) \rangle / \langle \delta H(t)^2 \rangle$ and the ω-dependent specific heat will be $C_p(\omega) = (V/k_B T^2) \int_0^\infty -(\mathrm{d}/\mathrm{d}t) \langle \delta H(t) \delta H(0) \rangle \mathrm{e}^{i\omega t} \mathrm{d}t$.

At temperatures at which the liquid $C_p(\omega)$ has a ω-dependence, there are two main contributions, one that equilibrates quickly and the other with an equilibration that slows increasely as dynamic arrest is approached.

In contrast to the traditional adiabatic method of measuring C_p (a short heat pulse applied to an isolated sample), experiments in the frequency domain are possible if we apply a ω-periodic energy power and measure the consequent T oscillations at that frequency. The experimental time must be longer than the sample thermal–diffusion time $\tau_D = C_p d^2/\kappa$ (with κ the thermal diffusivity and d the distance) and shorter than the time τ_d it takes the sample to decay at the surrounding heat bath temperature. Then $\tau_D \ll 1/\omega \ll \tau_d$.

The operation of these measurements is simple. The power dissipated in the heater has two components, a DC component (producing a constant temperature gradient in the cell) and a second component that oscillates at frequency ω (the origin of the diffusive thermal wave), $P(t) = (I_0^2 R/2)[1 + \cos(\omega t)]$, hence $T(\omega) = T_{DC} + T_\omega \cos(\omega t - \varphi)$, where T_{DC} is the heater average temperature and T_ω the oscillation amplitude. Typically this technique operates in the range $0.01 < f < 6\text{kHz}$, $(\omega = 2\pi f)$ [120].

The relationship between heat density q and heat current j_q in the heat-diffusion process is $\dot{q} + \nabla \cdot \mathbf{j}_q = 0$ and $\mathbf{j}_q = -\kappa \nabla T$ (where κ is the thermal conductivity), which combined give $\dot{q} = \kappa \nabla^2 T$. Considering that $\dot{q} = -i\omega q(\omega) = -i\omega C_p(\omega) T(\omega)$, then $-i\omega C_p(\omega) T(\omega) = \kappa \nabla^2 T$, the solutions of which depend on experimental geometry—the simplest being a plane [119] or a cylindrical [120] heater. The second geometry is the same as that of a DSC. Hence, temperature-modulated scanning calorimetry (TMSC), which consists of two identical cylindrical measuring cells, one empty and serving as a reference and the other containing the liquid sample, is a variant of the DSC. Using oscillating heating we obtain the components of the complex heat capacity ($C_p = C_p' - iC_p''$) oscillating in-phase, C_p', and out-of-phase, C_p'', with T during the $T(\omega)$ cycle. These components are related to the modulation amplitude and period, $1/f$. In terms of the linear response, the TMSC behaves as an electrical circuit with distributed loss and storage components.

In DSC heat capacity, C_p^{DSC} is measured from the rate of heat flow as $C_p^{DSC} = \beta^{-1} \mathrm{d}H(T, t, x_i)/\mathrm{d}t$, where $\mathrm{d}H(T, t, x_i)/\mathrm{d}t$ is the measured rate of enthalpy change and β is the temperature scanning (heating or cooling) rate. Considering $T = T(t)$, the material mole fraction x_i is

$$C_p^{DSC} = \left[\frac{\partial H}{\partial T} + \left(\frac{\partial H}{\partial x_i(T)}\right)\left(\frac{\mathrm{d}x_i}{\mathrm{d}T}\right)\right] + \left(\beta^{-1}\right)\left[\frac{\partial H}{\partial t} + \left(\frac{\partial H}{\partial x_i(t)}\right)\left(\frac{\mathrm{d}x_i}{\mathrm{d}t}\right)\right]. \tag{8}$$

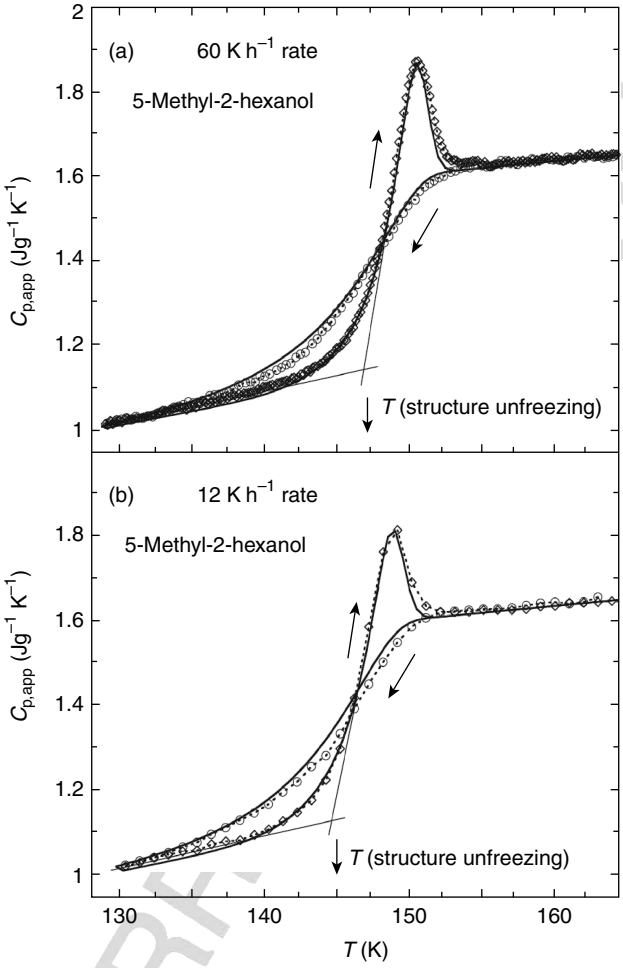

Figure 16. The specific heat measured in 5-methyl-2-hexanol in two different thermal rates (60 and 12K h^{-1}). The sample is first cooled and then heated [120].

Since $\partial H/\partial T = C_p$ is the true thermodynamic heat capacity at equilibrium, C_p^{DSC} accounts for it and all the other possible contributions caused by the nonequilibrium state of the system (or by the changes in its properties). For this reason C_p^{DSC} is also the apparent specific heat, that is, $C_p^{\mathrm{DSC}} = C_{p,\mathrm{app}}$. Figure 16 shows $C_{p,\mathrm{app}}$ results in 5-methyl-2-hexanol.

In terms of the last equation shown above three conditions are at the basis of enthalpy changes:

(a) When $(\partial H/\partial x_i) = 0$, or $(\mathrm{d}x_i/\mathrm{d}T) = 0$, $(\mathrm{d}x_i/\mathrm{d}t) = 0$ and $(\partial H/\partial t) = 0$, the measured value of C_p from a DSC experiment is given by $C_{p,\mathrm{app}} = C'_p = \partial H/\partial T$.

(b) When $(\partial H/\partial x_i) \neq 0$, or $(\mathrm{d}x_i/\mathrm{d}T) \neq 0$, but $(\mathrm{d}x_i/\mathrm{d}t) = 0$ and $(\partial Hh/\partial t) = 0$, that is, the fast reversible process restoring the original state of the sample at any time within the T modulation cycle is $C_{p,\mathrm{app}} = \partial H/\partial T + [\partial H/\partial x_i(T)](\partial x_i/\partial T) = C'_p$.

(c) When$(\partial H/\partial x_i) \neq 0$, or $(\mathrm{d}x_i/\mathrm{d}T) \neq 0$, $(\mathrm{d}x_i/\mathrm{d}t) \neq 0$ and $(\partial H/\partial t) \neq 0$, that is, because there are slow and irreversible chemical/physical processes occurring at that T, the original state is not restored during the modulation cycle and the time-dependent enthalpy is $C_{p,\mathrm{app}} \neq C'_p$.

Figure 17 shows this situation for 5-methyl-2-hexanol in the GT region and also reports the measured C''_p.

B. The Water Heat Capacity

As stated above, when water forms a glass its behavior is unusual. The system adsorbs or releases thermal energy as a function of thermodynamic variables, indicating the presence of an arrested phenomenon. At T_g the heat capacity detectably changes from a high-value characteristic of a liquid to a low-value characteristic of a solid, that is, its degree of freedom is only vibrational. Compared to other molecular liquids, water is also strange in this regard. The GT signature in the measured specific heat is so weak that the placement of its T_g is controversial [2,121], that is, it is possible that $130\mathrm{K} < T_\mathrm{g} < 160\mathrm{K}$ [122]. It is commonly known that glass-forming liquids, fall into two main classes, *fragile* and *strong* [123]. In fragile glass-forming liquids the change in heat capacity at T_g is sharp and is completed in just a few degrees. The relaxation time (τ) changes rapidly with temperature, in VFT fashion. In strong glass-forming liquids with high T_g values the change in heat capacity requires hundreds of degrees to complete the transition. Some consider water near its T_g to be a strong glass-forming liquid, but others consider it fragile [79].

There are two regions of the water phase diagram in which the specific heat C_p of bulk liquid water has been measured. Figure 18 shows the T-behavior of C_p measured down to 244.5K, where the obtained data fit the scaling law $C_p = A[(T - T_\mathrm{c})/T_\mathrm{c}]^{-x} + B$ (with $A = 0.44$, $B = 74.3$, $T_\mathrm{c} = 222\mathrm{K}$, and $x = 2.5$ [124].

Specific heat data are available in all temperature ranges except that in the No-Man's Land. In particular, data are available in the supercooled region ($T > 236\mathrm{K}$), in the region of H_2O vapor deposit (with $T_\mathrm{g} \sim 136\mathrm{K}$), and in the region of the hyperquenched (LDA) glassy water (estimated at $T_\mathrm{g} \sim 165\mathrm{K}$) [122]. Note that we can also find the T_g values of some molecular and ionic water solutions in this

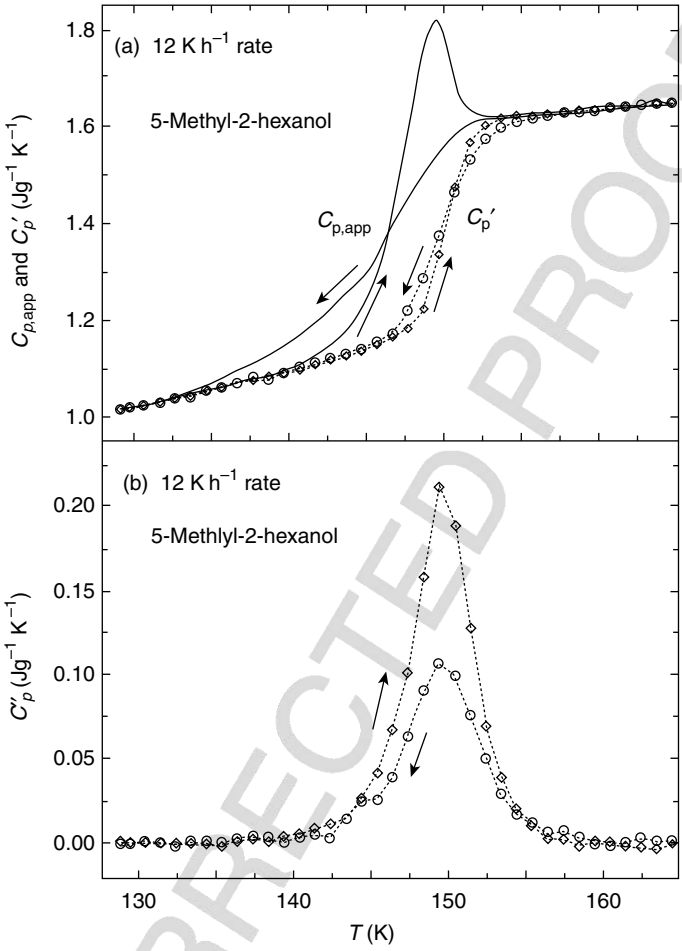

Figure 17. The real and imaginary parts of the specific heat measured during cooling and heating at a rate of 12K h^{-1} [120].

low T region. If we compare the calorimetric data measured in these solutions with the data measured in pure laboratory water, we find that the pure water ΔC_p is only 2% of that found in the solutions. In the case of a solution of hydrazine N_2H_4, we find $T_g \sim 140$K with $C_p \sim 75$J mol^{-1}K^{-1}, a value higher than that of LDA water [122] but lower than that in bulk water immediately below its freezing point. Calorimetric data of pure bulk water and confined water in an emulsion are about the same, tend to diverge, and fit a scaling law [124]. In emulsified water at the lowest studied temperature ($T = 236$K), we measured $C_p \sim 103$J mol^{-1}K^{-1}. This is one example of what can be found in the No-Man's Land region. We can

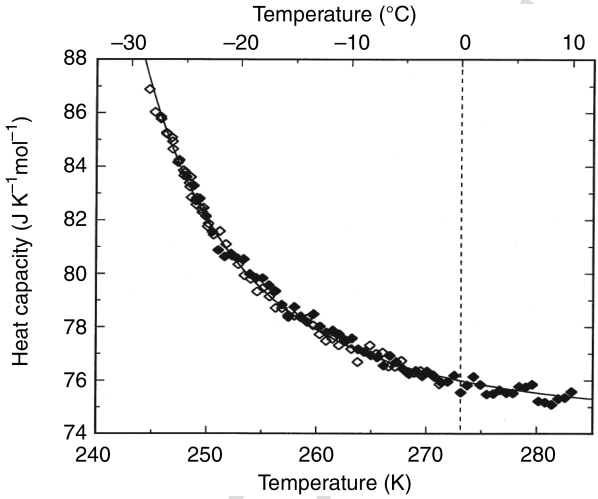

Figure 18. Heat capacity of bulk water [124].

look for behaviors along a continuous $C_p(T)$ path between the large and diverging value of the supercooled liquid phase, and the tiny value at 130–150K.

Many calorimetric experiments on confined water in the very supercooled regime have been carried out [125–127]. Recently the heat capacity of nanoscopically confined water was measured using the adiabatic method [128,129] inside the No-Man's Land. This technique is particularly appropriate because in water the specific heat jump (connected with the GT) is small or occurs over a wide T range. The method is based on the specific properties of a glass as it ages, and involves directly observing the enthalpy relaxations at different thermal rates. In these experiments different confining materials like silica gels [128] and nanotubes [129] of different pore sizes have been used in order to separate the "surface" water properties from those of "internal" water.

The first adiabatic study was carried out for H_2O and D_2O water confined within the voids of silica-gel materials with average pore diameters in the range $1.1 < \phi < 52$ nm [128]. Most of the water was found to crystallize within pores that were $\phi > 2$ nm in diameter, but for $\phi \leq 2$ nm it remained in the liquid state down to 80K. In particular, it was found that internal water undergoes a GT at 160 and 165K for ordinary and heavy water, respectively, and that the interfacial water on the pore wall that exhibits a GT over the range 115–139K has only one layer. Thus, due to the development of an energetically more stable HB network of water molecules at low T, the GT of bulk supercooled water takes place at $\geq$160K.

Although it is difficult to identify T_g in water, it is nevertheless interesting, after the TMSC [130], to also measure adiabatic calorimeters. These measurements are usually carried out by intermittently heating or cooling the sample under adiabatic

conditions. The temperature of the sample is increased at a rate R by means of power P from an initial temperature T_i to a final temperature T_f. The heat capacity is thus $C_p = P/(T_f - T_i)$. When the sample absorbs or releases heat when it reaches the equilibrium state, we see a spontaneous temperature drift dT/dt. The enthalpy relaxation rate is then evaluated by $(-dH/dt) = C_p(dT/dt)$.

As the configurational enthalpy approaches GT, it decreases with T and the molecular configurational relaxation time τ increases. When the configurational enthalpy reaches GT, the nonequilibrium relaxations change from nonequilibrium to equilibrium. Due to the nonergodicity, the nonequilibrium states at a certain constant T and the corresponding $(-dH/dt)$ relaxations are strongly dependent on the thermal history of the sample, for example, the pre-cooling rate (Fig. 19).

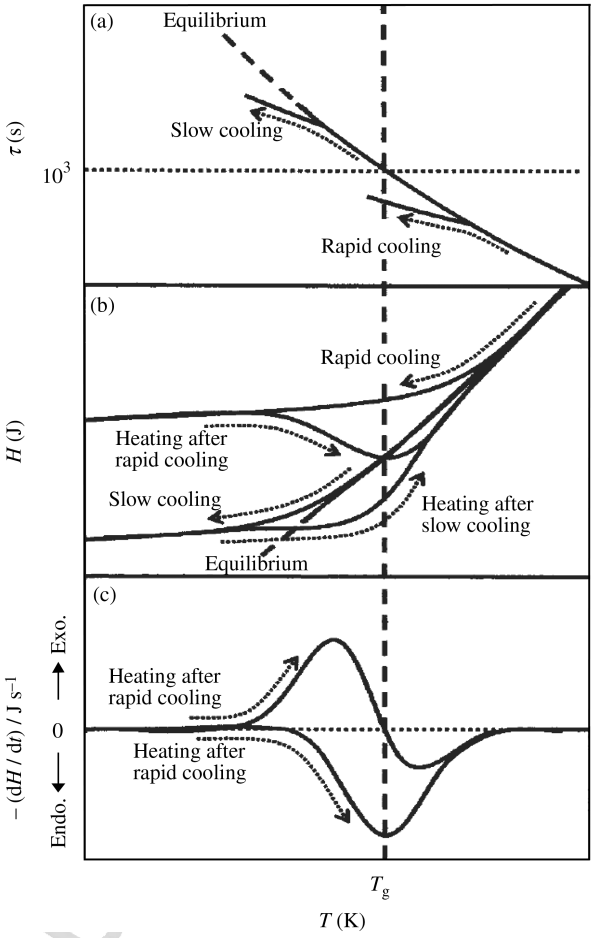

Figure 19. Relationship between the relaxation time τ, the enthalpy H, and the spontaneous enthalpy relaxation rate $-dH/dt$ observed in the dynamic arrest region. T_g was determined empirically as the point at which the rapidly cooled sample showed a change (against T) in dH/dt from positive to negative and the slowly cooled sample showed a minimum dH/dt value [131].

When the liquid vitrifies through rapid cooling, τ deviates from the equilibrium dependence at relatively high T, and H becomes much higher than it was in the equilibrium situation (Fig. 19a). This rapid cooling (or quenching) freezes the configurational structure such that it corresponds to one at high T, and the enthalpy will be higher than it was in the equilibrium situation (Fig. 19b). The reverse is true when T of the glass is increased, that is, τ becomes short and gradually approaches an observable timescale (e.g., $10^2 < \tau < 10^6$ s). This increase in T corresponds to the case in which H begins to relax and decrease toward its equilibrium value and we see an exothermic enthalpy relaxation effect. Because of the shortening of τ (Fig. 19c), $-\mathrm{d}H/\mathrm{d}t$ increases with an increase in temperature. A further increase in T happens when H crosses the equilibrium line near T_g and takes on values smaller when it was at equilibrium. We see $-\mathrm{d}H/\mathrm{d}t$ exhibit a positive peak, become zero as H crosses the equilibrium line, and then take on negative values (Fig. 19c). As we increase the temperature further, τ becomes increasingly short and the liquid exhibits no relaxation phenomenon on the experimental timescale. Consequently $\mathrm{d}H/\mathrm{d}t$ returns to zero as the glass reaches its equilibrium state.

If we cool the liquid very slowly and it vitrifies, τ and H deviate from their respective equilibrium lines at a T' that is relatively lower—and an H that is considerably lower—than when the cooling was rapid. When we heat the liquid, an endothermic enthalpy relaxation appears after H crosses the equilibrium line, takes on lower values than when it was at equilibrium, and $-\mathrm{d}H/\mathrm{d}t$ exhibits a negative peak. As τ becomes shorter with increasing T, H gradually returns to the equilibrium line at approximately the same T as when the liquid was cooled rapidly. Depending on the precooling rates, a kind of hysteresis loop is exhibited in the relaxation rates—which is the calorimetric characteristic of a GT. It has the same physical origin as the phenomena characterizing the aging processes. These observations of a set of exothermic and endothermic $-\mathrm{d}H/\mathrm{d}t$ values for the rapidly and slowly cooled samples, respectively, indicate the presence of a GT. The T_g value is empirically determined to be the temperature at which the rapidly cooled sample shows a change in $-\mathrm{d}H/\mathrm{d}t$ from heat-evolution to heat-absorption effects, and the slowly cooled sample shows a maximum in the heat-absorption effect [131]. In the case of vitrified ice in particular, well defined maxima are observed in the C_p/T at different temperatures (around 110K) depending on the treatment of the samples.

We can use this same technique to separately measure the H relaxation rate $-\mathrm{d}H/\mathrm{d}t$ or the rate of spontaneous heat release or absorption in water confined in silica-gel materials [128] and MCM-41 nanopores [132]. The rate of spontaneous heat release or absorption, in the thermometry periods of heat-capacity measurements upon intermittent heating, gives the correct indication of the water T_g. In these experiments the enthalpy relaxation $-\mathrm{d}H/\mathrm{d}t$ is $-\mathrm{d}H/\mathrm{d}t = C_p(\mathrm{d}T/\mathrm{d}t)/n_W$, where C_p is the measured heat capacity and n_W is the amount of water within the pores. In both H_2O and D_2O, when the sample was cooled rapidly in this

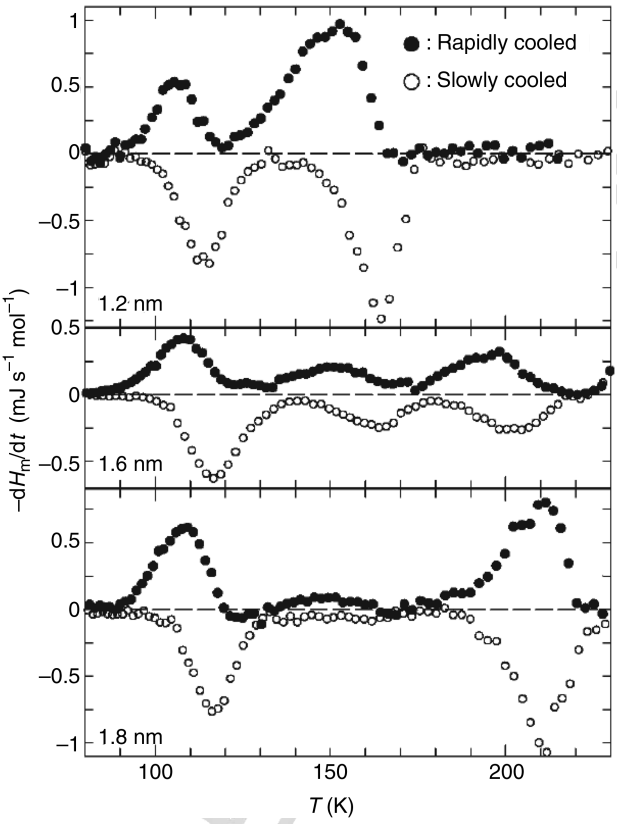

Figure 20. Spontaneous enthalpy release and absorption rates of the water confined within nanopores of silica MCM-41 with different pore diameters [132].

temperature range before measurement, heat-release (positive $-\mathrm{d}H/\mathrm{d}t$) and then heat-absorption (negative $\mathrm{d}H/\mathrm{d}t$) effects were observed. When the sample was cooled slowly, on the other hand, only the heat-absorption effect was observed. This dependence reflects the enthalpy relaxation of the water caused by its structural change and is characteristic of a GT as described above.

Note that C_p exhibits a very large dominant peak. Calorimetry was performed in the heating direction, repeating the energy supply and thermometry periods under adiabatic conditions. Figures 20 and 21 show the MCM sample with $\phi =$ 1.2, 1.6, and 1.8 pore sizes for $-\mathrm{d}H/\mathrm{d}t$ and C_p. Figure 21 also shows, for the sake of comparison, the specific heat data of ice (dashed line) and bulk water ($T \geq 270$K) [132].

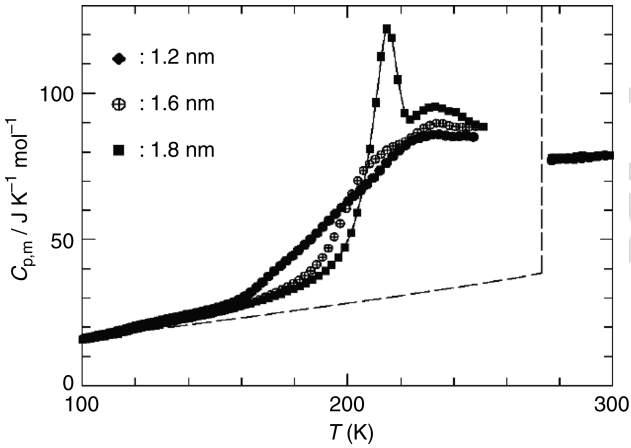

Figure 21. The molar heat capacity $C_{p,\mathrm{m}}$ measured in water confined in silica nanotubes (MCM-41 ϕ =1.2, 1.6, and 1.8nm) [132].

Figure 21 shows that crystallization occurs when the silica nanotubes are 1.8 nm in diameter, and that water remains liquid up to $\approx$ 160K when the nanotubes are 1.2 and 1.6 nm in diameter. Our previous analysis of water confined in silica gels revealed glass transitions at about 115 and 165K and in the case of water confined in 1.6 nm pores at about 205K. Figure 22 shows data from water confined in silica-gel voids of $\phi = 1.1$ nm, and also data on emulsified water.

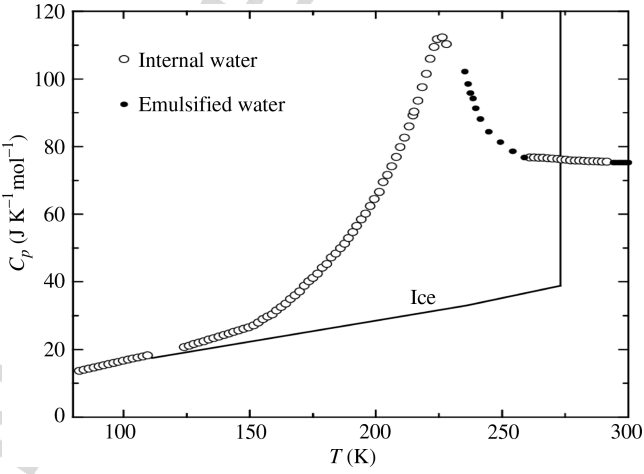

Figure 22. Heat capacity of internal water, emulsified water, and ice [122,132].

Going under the assumption that the form of the excess $C_p(T)$ reported in these latter experiments differs completely from that in common glass formers, but resembles that of the classical order–disorder transition, an interesting analysis of these calorimetric data of nanoconfined water has been proposed [122]. Note that the order–disorder transition (critical point-free) scenario differs little from the second critical point scenario, which attributes all water anomalies to the existence of a second critical point.

The important question remains: is this second critical point the key to understanding the anomalies of water, or does the cooperation of the configurational excitations at some parameter or some thermodynamic field choice produce a critical point? The cooperation of the configurational excitation is implied by the form of the heat capacity extracted by confined water, in particular, that of water confined in silica-gel materials [128] at $\phi = 1.1$ nm. In this case, water remains in the liquid state at very low T and shows a C_p peak at approximately 227K (see, e.g., Fig. 21). The hump at 227K supports the order–disorder process hypothesis of water molecules in the liquid state. This silica-gel sample $-\mathrm{d}H/\mathrm{d}t$ does not give a water GT at this temperature, the 227K peak can be attributed to an order–disorder process, and the T_g is located at lower temperatures.

Figure 23 shows the results of a recent TMSC experiment in MCM-41-S confined water with $\phi = 2.4$ and 1.8 nm. Note that there is a close similarity between these data and the data obtained from adiabatic calorimetry. Their interpretation, however, is completely different. Taking into account the results obtained for the water transport coefficients, represented by the NMR and neutron data, the results obtained for the dynamic fragile-to-strong glass crossover (Fig. 9), and the violation of the Stokes–Einstein relation (Fig. 10) we can assume that these maxima in C_p at about 225K are related to the crossover phenomenon and not a GT process.

Taking into account the results of the FTIR experiments (see, e.g., Figs. 11 and 12), we can also assume that these maxima are caused by water polymorphism, more precisely by the change in the relative populations of the high-density and low-density liquid water phases that takes place at the crossover temperature $T_\mathrm{L} \simeq$ 225K. This approach has been confirmed by a consideration of the configurational contribution to the specific heat (see next section).

VIII. THE NMR AND THE CONFIGURATIONAL HEAT CAPACITY

We now use the NMR chemical shift to measure the configurational specific heat of a material. This experimental approach can give detailed information on water inside the very supercooled regime, and focuses on confined water in nanotubes and in macromolecules of biological interest [133].

Scattering experiments using neutrons and X-rays have given precise values for the PCF, and thus provided important benchmarks for testing models

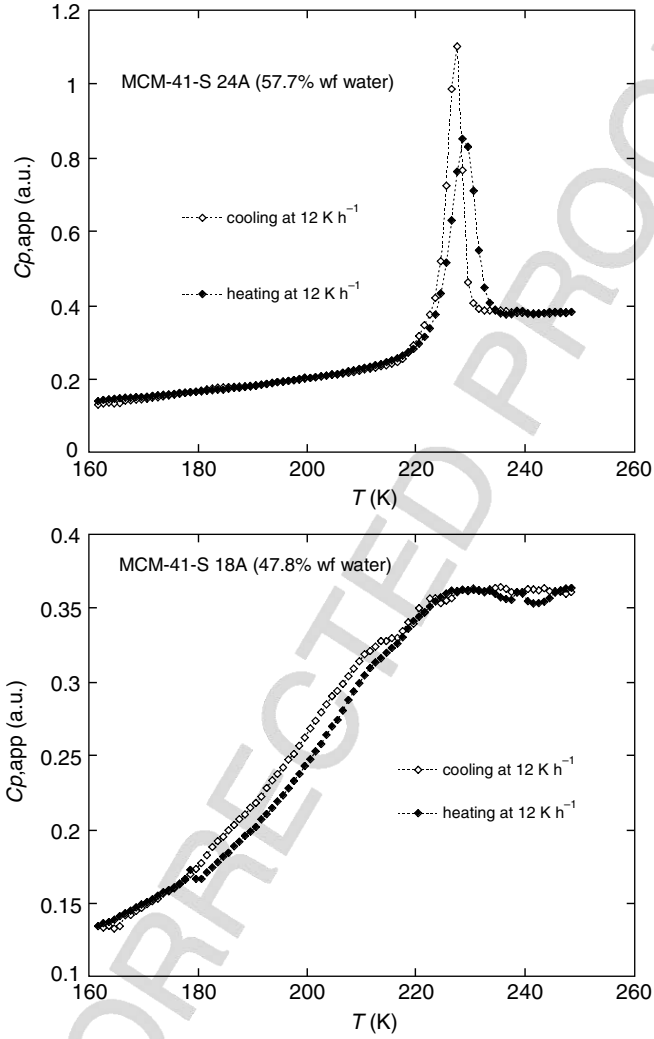

Figure 23. The specific heat $C_{p,\mathrm{app}}$ in MCM-41-S confined water measured by using a modulated calorimeter. The tube diameters are 2.4 nm (upper) and 1.8 nm (lower).

of water structure. Because the PCF represents only an isotropically averaged measure of the structure, in many cases PCFs may not faithfully reproduce the subtle hydrogen bond geometry responsible for water's thermal anomalies. By measuring the NMR proton chemical shift δ it is possible to provide additional information on the local hydrogen bond geometry and, in particular, the average

number of the possible configurations ($\langle N_{\mathrm{HB}} \rangle$) of the local molecular hydrogen bonding geometry. If a water molecule in a dilute gas is taken to be an isolated-state benchmark, the chemical shift δ accounts for the change of the value of the magnetic shielding with respect to that benchmark. Hence, the chemical shift is related to the interaction of a water molecule with its surroundings, providing a picture of the intermolecular geometry [134–136]. It was originally proposed that δ corresponds to the number of hydrogen bonds (HB), N_{HB}, each water molecule has, especially for the highest T [137]. After many theoretical and experimental studies it is now assumed that the proton chemical shift in water is a function not only of the number of HBs but also of the intermolecular distances and angles, that is, $\langle N_{\mathrm{HB}} \rangle$ [135]. Thus, a careful study of δ versus T gives details of the thermal evolution of water configurations, especially in the supercooled regime where an onset of complex clustering phenomena occurs (similar to percolation [21]) driven solely by the HB interaction [7,9,19,42]. Here we study confined water in quasi-1D cylindrical tubes (MCM-41-S) and find that the T derivative of the chemical shift can give an estimate of the configurational specific heat and measure the water proton chemical shift as a function of temperature [46,54,75,87,88].

We assume that the NMR chemical shift δ is a linear response of the electronic structure of a system to an external magnetic field B_0, as $B(j) = (1 - \delta_j)B_0$, where j is an index identifying the chemical environment [138,139]. We measured it in an NMR experiment using FID. The NMR technique was originally used only to accurately measure the nuclear magnetic moment. After the discovery of the chemical shift effect, the technique was utilized by the chemical physics community and it was found that FID yields information about the set of all nuclear species in the studied sample whose resonance frequencies lie within the harmonic content of the NMR radio frequency (RF) pulse. Thus, NMR, by means of chemical shift δ, is selective of the nucleus chosen to be studied and is highly sensitive to its local environment. In particular, the FID is related to the magnetic shielding tensor σ, which in turn is related to the local field experienced by the magnetic moment of the nucleus. The magnetic shielding tensor σ is strongly dependent on the local electronic environment and can be used to probe the local geometry, in particular, the hydrogen bond structure of water and aqueous systems and solutions. Of particular interest are the isotropic part, $\sigma_{\mathrm{iso}} \equiv \mathrm{Tr}(\sigma/3)$, and the shielding anisotropy $\Delta\sigma \equiv \sigma_{33} - (\sigma_{11} + \sigma_{22})/2$, where σ_{11}, σ_{22}, and σ_{33} are the three principal components of σ. σ_{iso} is experimentally obtained via the measured proton chemical shift relative to a reference state through the relation [140]

$$\delta = \sigma_{\mathrm{iso}}^{\mathrm{ref}} - \sigma_{\mathrm{iso}} + \left(A - \frac{1}{3}\right)(\chi^{\mathrm{ref}} - \chi) \tag{9}$$

Here χ is the magnetic susceptibility, and the factor A depends on the sample shape and orientation, for example, $A = 1/3$ for a spherical sample. Since the magnetic

field exerted on a proton is $B_0[1 + (4\pi/3)\chi(T)]$, the resonance frequency is $\omega(T) = \gamma H_0[1 - \sigma(T) + (4\pi/3)\chi(T)]$, where γ is the proton gyromagnetic ratio. Thus, the deviation of $\sigma(T)$ from a reference value gives $\delta(T)$. Since the magnetic susceptibility for each water molecule, χ_0, can be assumed to be T and P independent, $\chi(T)$ is given by $\chi_0\rho(T)$, where $\rho(T)$ is the density at temperature T. In the liquid and gas phases, $\omega(T)$ and $\rho(T)$ can be obtained experimentally. Because water molecules in the gas phase at 473K are isolated, we can set $\delta_g(473\text{K}) = 0$, where g designates the gas. Thus, $\delta(T) = (\omega(T) - \omega_g)/\omega_g - (4\pi/3)\chi_0(\rho(T) - \rho_g)$, which is determined from $\omega(T)$ and $\rho(T)$. Thus an isolated water molecule in a dilute gas can be used as a reference for δ, and δ then can provide a rigorous picture of the intermolecular geometry [134] portraying how water molecules interact with their surroundings. In liquid water, fast molecular tumbling is used to isotropically average the shielding tensor, so the NMR frequency only provides information on σ_{iso}. We also cannot detect the $\Delta\sigma$ contribution because the ^{1}H relaxation is strongly affected by the magnetic dipole field from nearby protons [140]. However, δ is directly related to the average number of local configurations in which a water molecule is involved [134,135]. The water proton chemical shift has also been studied in a confined geometry using tube diameters of $d = 2.4$ and 1.4 nm [88]. Both diameters yield hydration levels of $h \simeq 0.5$. In this case static NMR experiments at ambient pressure in the temperature interval $195\text{K} < T < 293\text{K}$ using the NMR spectrometer of the self-diffusion experiment.

Figure 24 shows our $\delta(T)$ data in MCM samples (corrected for the magnetic susceptibility $\chi(T) = \chi_0\rho(T)$), all the experimentally available $\delta(T)$ data in the

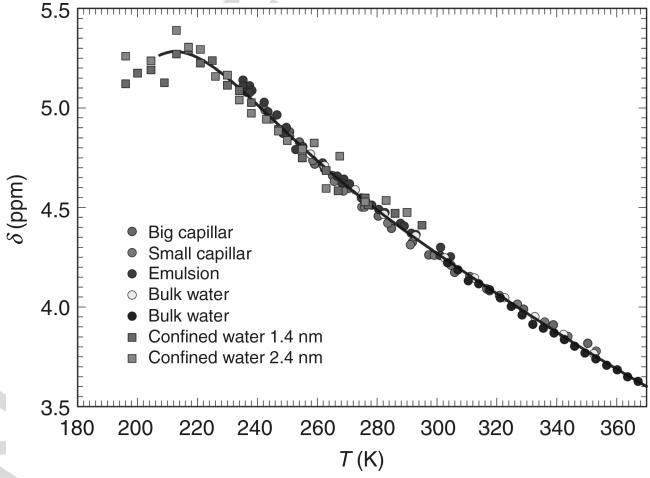

Figure 24. The temperature behavior of the water proton chemical shift δ. Our data (squares) and data from the literature (circles) [133].

temperature range of stable bulk liquid water, and the δ values from $T = 350$K down to 235K of three different samples: large capillaries (80–120 μm) [137], small capillaries (10–20 μm) [137], and water confined in an emulsion [141]. Although the reference material for the δ data of Refs [137,141] is CH_4, all the measured values after correction fall on a single curve for which the reference system is a water molecule in a diluted gas under supercritical conditions [134]. Figure 24 shows this for $180\text{K} < T < 370\text{K}$ and shows agreement between our data and the previous $\delta(T)$ measurements. Note that these data from the literature (circles) show a continuous increase on decreasing T that becomes more pronounced in the low-temperature region. There is a round-off in $\delta(T)$ with a possible maximum at approximately 215K. With respect to an isolated water molecule, different experiments quote $\delta = 7.4$ ppm for a single crystal of hexagonal ice I_h [142] and the data show that $\delta(T)$ does not evolve in a simple monotonic way from the liquid to the ice phase. The continuous increase in the proton chemical shift, with T decreasing down to the supercooled regime, was originally understood to be a cooperative increase in HB formation rate. Thus, there is a rapid increase in short-range order or "clustering." The T region below 225K is dominated by the LDL local structure [88], confirming that this liquid water phase has a local geometry that differs from the HDL local structure prevalent in the stable liquid regime.

In terms of the reported FTIR data, Fig. 24 shows the relative population of LDL-like and HDL-like local structures [88,106] in the region $30\text{K} < T < 373\text{K}$, thus providing a qualitative explanation for the observed $\delta(T)$. Structurally the temperature range can be divided into three sections: (i) $\mathcal{R}_{\text{HDL}}$ ($T > 250$K) dominated by molecules with local HDL geometry, (ii) $\mathcal{R}_{\text{LDL}}$ ($T \lesssim 220$K) dominated by local LDL geometry with an intermediate region in which the population of these local geometries are comparable, and (iii) $\mathcal{R}_{\text{int}}$ ($220\text{K} \lesssim T < 250\text{K}$).

Note that as the temperature decreases $\delta(T)$ shows three different behaviors in the three different regions: (i) a continuous increase in $\mathcal{R}_{\text{HDL}}$, (ii) an inflection point at approximately 250K with a sudden change in the derivative in the $\mathcal{R}_{\text{int}}$ interval, and (iii) a flattening at approximately 220K followed by a slow decrease in the $\mathcal{R}_{\text{LDL}}$ region. These results confirm the main role played by the LDL and HDL local geometric structure characterized by different local electronic distributions, and thus by different local environments of the hydrogen atom. A analysis of their fractional weights allows us to calculate the absolute water density value $\rho(T)$ in the range $30\text{K} < T < 373\text{K}$. In addition to the well-known maximum at 277K, there is a minimum in $\rho(T)$ at 203 ± 5K [106]. The coefficient of thermal expansion $\alpha_\rho = -(\partial\rho/\partial T)_p$, related to the cross-correlation between the entropy and volume fluctuations, shows a well-defined maximum on crossing the Widom line $T_W(P)$. In the first interval $\mathcal{R}_{\text{HDL}}$, where the normal liquid region (273–353K) and a region of moderate supercooling are located, $\delta(T)$ increases as T decreases. Our consideration of the normal liquid region and the supercritical region is both theoretical and experimental. We find that the proton chemical shift

reflects the properties of the local order [134,135] in regions in which there is a direct relation between $\delta(T)$ and the average number of hydrogen bonds $\langle N_{\rm HB}\rangle$ each water molecule has, that is, $\delta(T) \propto \langle N_{\rm HB}\rangle$. We apply the thermal evolution of the LDL and HDL local structures (Fig. 24) to the other two temperature regions, $\mathcal{R}_{\rm int}$ and $\mathcal{R}_{\rm LDL}$. In both regions the tetrahedral HB network expands as the temperature decreases.

$\delta(T)$ is related to the number of possible configurations of the water molecules in the HB network. Since this number is inversely proportional to $\langle N_{\rm HB}\rangle$, the definition of entropy allows us to assume $S \approx -k_{\rm B} \ln\langle N_{\rm HB}\rangle$. Thus, the T derivative of the measured fractional chemical shift,

$$-\left(\frac{\partial \ln \delta(T)}{\partial T}\right)_p \approx -\left(\frac{\partial \ln\langle N_{\rm HB}\rangle}{\partial T}\right)_p \approx \left(\frac{\partial S}{\partial T}\right)_p \tag{10}$$

should be proportional to the constant pressure specific heat $C_p(T)$ ($C_p = T(\partial S/\partial T)_p$), a quantity that has never been experimentally measured in the deep supercooled regime below 250K in liquid bulk water.

The left-hand side of Fig. 25 shows the derivative $-T\partial \ln \delta(T)/\partial T$ obtained from $\delta(T)$ data [133]. Also shown are the $C_p(T)$ values measured in bulk water in the interval 244.5K $< T <$ 290K [124] and the same quantity obtained by means of a simulation study from the TIP5P model of water for 210K $< T <$ 290K (right-hand side) [143].

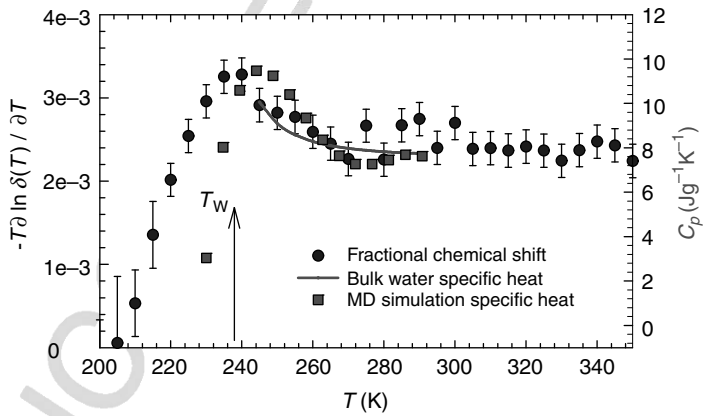

Figure 25. The temperature derivative of the measured fractional chemical shift $-T\partial \ln \delta(T)/\partial T$ (solid circles, left-hand side), the specific heat at constant pressure, C_p (right-hand side), measured in bulk water in the supercooled regime (solid line, Ref. [124]), and C_p calculated for the TIP5P model of water (solid squares, Ref. [143]).

All these data display an analogous thermal behavior and, within the error bars, there is good agreement between the C_p data. The "configurational" specific heat obtained from the measured δ and the $C_p(T)$ calculated using simulations display maxima at approximately the same temperature ($\simeq$ 235K) as the maximum in $(\partial\rho/\partial T)_p$ [106] upon crossing the Widom line temperature, T_W [87,144]. Whereas $(\partial\rho/\partial T)_p$ is directly related to the cross-correlation between the entropy and volume fluctuations $\langle(\Delta S \Delta V)\rangle$, C_p is proportional to the square of the entropy fluctuations. Note that very recent calorimetric data on water confined in silica gel in the range 100K $< T <$ 300K show a behavior that agrees with our results [129].

We conclude that NMR proton chemical shift measurements may provide a new way to estimate the configurational component of the heat capacity $C_p(T)$ that is the result of the hydrogen bonding of water molecules. Because the NMR technique also gives the chemical shift of each sample nucleus with a nonzero spin, it may also be applicable to more complex materials.

IX. CONCLUDING REMARKS

In our wide survey of confined water research, we have examined both experimental and theoretical studies and have highlighted recent discoveries that strongly indicate that confined water will soon enable us to effective examine the No-Man's Land below the supercooled region. Our most important results indicate (i) the existence of a dynamic crossover FSC at a precise temperature, (ii) the existence of the Widom line $T_W(p)$, (iii) the breakdown of the Stokes–Einstein relation for $T < T_W(p)$ [87,144–146], (iv) the coincidence that the FSC singularity with the BSE occurs at the same T_W gives support to the LLPT theory that liquid water consists of a mixture of two differing local liquid structures (the LDL and HDL phases), (v) that there are systematic changes in the static structure factor $S(q)$ and the corresponding pair correlation function $g(r)$, which reveal that for $T < T_W(p)$ the system resembles more the structure of LDL than HDL, (vi) the appearance for $T < T_W(p)$ of a shoulder in the dynamic structure factor $S(q, \omega)$ at a frequency $\omega \approx 60$ cm$^{-1} \approx 2$ THz [90], (vii) the rapid increase in the degree of hydrogen bonding for $T < T_W(p)$ [86], (viii) a *minimum* in the density at low temperature [91,106], (ix) a scaled equation of state near the critical point [92], and (x) a clear maximum in the coefficient of thermal expansion at $T_W \approx 225$K [106,133], which remarkably is the same temperature as the specific heat maxima, is the one measured with conventional calorimetry [128], and is the second one obtained by NMR [133]. It is possible that the phenomena that appear to occur on crossing the Widom line are in fact not coincidences, but are related to the changes in local structure that occur when the system changes from the "HDL-like" side to the "LDL-like" side. In this work, we have reviewed the evidence for changes in such dynamic transport properties as the diffusion constant and the relaxation

time. Because these phenomena are evident only in confined water and cannot be explored in bulk water, it is possible that the physics of bulk water will differ significantly.

Of paramount importance are the two crossover phenomena observed in protein hydration water, which, on the basis of the many results we have described, can be considered responsible for the biological activity of macromolecules, including RNA and DNA. Neutron measurements of the MSD indicate, surprisingly, that the crossover temperature of biopolymer and its hydration water are closely synchronized. More precisely, FTIR experiments indicate that when a biosystem restores its dynamics, the solvent crosses from a strong to a fragile liquid, that is, the HB networking changes from a thermal state in which LDL dominates to one in which HDL dominates. At the same time, irreversible denaturation takes place when the HB numbers decrease to the point at which only a few water molecules are bonded.

ACKNOWLEDGMENTS

Research in Messina is supported by the PRIN2008. Research at Boston University is supported by National Science Foundation Chemistry Division Grants CHE0616489, CHE0908218, and CHE0911389. This work utilized facilities supported in part by the National Science Foundation under Agreement DMR-0086210. We acknowledge the corresponding publishers for the permissions to reproduce figures 2, 5, 8–13, 19, 21–25.

REFERENCES

1. F. Mallamace and H. E. Stanley, *Proceedings of the International School of Physics "Enrico Fermi"* (Varenna, 1996), F. Mallamace and H.E. Stanley, eds., IOS Press, Amsterdam, 1997; F. Mallamace and H.E. Stanley, *The Physics of Complex Systems (New Advances and Perspectives)*, F. Mallamace and H. E. Stanley, eds., IOS Press, Amsterdam, 2004.
2. P. G. Debenedetti and H. E. Stanley, *Phys. Today* **56**, 40 (2003).
3. O. Mishima and H. E. Stanley, *Nature* **396**, 329 (1998).
4. R. J. Speedy and C. A. Angell, *J. Chem. Phys.* **65**, 851 (1976).
5. G. S. Kell, *J. Chem. Eng. Data* **12**, 66 (1967); G. S. Kell, *J. Chem. Eng. Data* **20**, 97 (1975).
6. F. Sciortino, P. Poole, H. E. Stanley, and S. Havlin, *Phys. Rev. Lett.* **64**, 1686 (1990).
7. O. Mishima, L. D. Calvert, and E. Whalley, *Nature* **310**, 393 (1984); O. Mishima, L. D. Calvert, and E. Whalley, *Nature* **314**, 76 (1985).
8. O. Mishima, *Nature* **384**, 546 (1996).
9. E. F. Burton and W. F. Oliver, *Proc. R. Soc. London Ser.* **153**, 166 (1936).
10. M.-C. Bellissent-Funel, et al., *J. Chem. Phys.* **97**, 1282 (1992).
11. P. H. Poole, T. Grande, F. Sciortino, H. E. Stanley, and C. A. Angell, *J. Comp. Matter Sci.* **4**, 373 (1995).
12. J. L. Finney, et al., *Phys. Rev. Lett.* **89**, 503 (2002).

13. I. Brovchenko, A. Geiger, and A. Oleinikova, *J. Chem. Phys.* **118**, 9473 (2003).
14. J. L. Finney, A. Hallbrucker, I. Kohl, A. K. Soper, and D. T. Bowron, *Phys. Rev. Lett.* **88**, 225503 (2002).
15. V. Velikov, S. Borick, and C. A. Angell, *Science* **294**, 2335 (2001).
16. D. Eisenberg and W. Kauzmann, *The Structure and Properties of Water*, Oxford University Press, New York, 1969.
17. J. D. Bernal and R. H. Fowler, *J. Chem. Phys.* **1**, 515 (1933).
18. L. Pauling, The structure of water, in *Hydrogen Bonding*, D. Hadzi, ed., Pergamon Press, New York, 1959, pp. 1–5.
19. R. J. Speedy, *J. Phys. Chem.* **86**, 982 (1982).
20. S. Sastry, P. Debenedetti, F. Sciortino, and H. E. Stanley, *Phys. Rev. E* **53**, 6144 (1996).
21. H. E. Stanley and J. Teixeira, *J. Chem. Phys.* **73**, 3404 (1980).
22. H. E. Stanley, *J. Phys. A* **12**, L329 (1979).
23. A. Geiger and H. E. Stanley, *Phys. Rev. Lett.* **49**, 1749 (1982).
24. J. R. Errington, P. G. Debenedetti, and S. Torquato, *Phys. Rev. Lett.* **89**, 215503 (2002).
25. P. H. Poole, F. Sciortino, U. Essmann, and H. E. Stanley, *Nature* **360**, 2002 (1992).
26. E. G. Ponyatovskii, V. V. Sinitsyn, and T. A. Pozdnyakova, *JETP Lett.* **60**, 360 (1994).
27. P. H. Poole, F. Sciortino, T. Grande, H. E. Stanley, and C. A. Angell, *Phys. Rev. Lett.* **73**, 1632 (1994).
28. S. S. Borick, P. G. Debenedetti, and S. Sastry, *J. Phys. Chem.* **99**, 3781 (1995).
29. G. Franzese and H. E. Stanley, *Physica A* **314**, 508 (2002).
30. E. Trinh and R. E. Apfel, *J. Chem. Phys.* **72**, 6731 (1980).
31. J. M. H. Levelt, measurements of the compressibility of argon in the gaseous and liquid phase, Ph.D. thesis, University of Amsterdam, Van Gorkum and Co., 1958.
32. H. Kanno, R. Speedy, and C. A. Angell, *Science* **189**, 880 (1975).
33. O. Mishima and H. E. Stanley, *Nature* **392**, 164 (1998).
34. R. J. Speedy, et al., *J. Chem. Phys.* **105**, 240 (1996).
35. P. Brüggeller and E. Mayer, *Nature* **288**, 569 (1980).
36. S. Harrington et al., *Phys. Rev. Lett.* **78**, 2409 (1997); *J. Chem. Phys.* **107**, 7443 (1997).
37. F. Sciortino, P. H. Poole, U. Essmann, and H. E. Stanley, *Phys. Rev. E* **55**, 727 (1997).
38. M. Yamada, S. Mossa, H. E. Stanley, and F. Sciortino, *Phys. Rev. Lett.* **88**, 195701 (2002).
39. D. Paschek, *Phys. Rev. Lett.* **94**, 217802 (2005).
40. E. Shiratani and M. Sasai, *J. Chem. Phys.* **108**, 3264 (1998).
41. H. E. Stanley, et al., *Phys. Chem. Chem. Phys.* **2**, 1551 (2000).
42. A. K. Soper and M. A. Ricci, *Phys. Rev. Lett.* **84**, 2881 (2000) and references cited therein.
43. R. Zangi and A. E. Mark, *J. Chem. Phys.* **119**, 1694 (2003).
44. M.-C. Bellissent-Funel, J.-M. Zanotti, and S.-H. Chen, *Faraday Discuss.* **103**, 281 (1996).
45. T. M. Truskett, P. G. Debenedetti, and S. Torquato, *J. Chem. Phys.* **114**, 2401 (2001).
46. L. Liu, S.-H. Chen, A. Faraone, C.-W. Yen, and C.-Y. Mou, *Phys. Rev. Lett.* **95**, 117802 (2005).
47. K. Koga, X. C. Zeng, and H. Tanaka, *Nature* **408**, 564 (2000).
48. R. Bergman and J. Swenson, *Nature* **403**, 283 (2000).
49. P. Gallo, M. Rovere, M. A. Ricci, C. Hartnig, and E. Spohr, *Europhys. Lett.* **49**, 183 (2000).

50. M. Meyer and H. E. Stanley, *J. Phys. Chem. B* **103**, 9728 (1999).
51. J. M. Zanotti, M.-C. Bellissent-Funel, and S.-H. Chen, *Phys. Rev. E* **59**, 3084 (1999).
52. H. Tanaka, R. Yamamoto, K. Koga, and X. C. Zeng, *Chem. Phys. Lett.* **304**, 378 (1999).
53. G. T. Gao, X. C. Zeng, and H. Tanaka, *J. Chem. Phys.* **112**, 8534 (2000).
54. L. Xu, et al., *Proc. Natl. Acad. Sci. USA* **102**, 16558 (2005).
55. P. C. Hemmer and G. Stell, *Phys. Rev. Lett.* **24**, 1284 (1970).
56. S. Sastry, F. Sciortino, and H. E. Stanley, *J. Chem. Phys.* **98**, 9863 (1993).
57. C. J. Roberts, A. Z. Panagiotopulos, and P. G. Debenedetti, *Phys. Rev. Lett.* **77**, 4386 (1996).
58. G. Franzese, G. Malescio, A. Skibinsky, S. V. Buldyrev, and H. E. Stanley, *Nature* **409**, 692 (2001).
59. C. A. Angell, J. Shuppert, and J. C. Tucker, *J. Phys. Chem.* **77**, 3092 (1973).
60. F. Sciortino, P. Gallo, P. Tartaglia, and S.-H. Chen, *Phys. Rev. E* **54**, 6331 (1996).
61. Y. Xie, K. F. Ludwig, G. Morales, D. E. Hare, and C. M. Sorensen, *Phys. Rev. Lett.* **71**, 2051 (1993).
62. F. W. Starr, J. K. Nielsen, and H. E. Stanley, *Phys. Rev. Lett.* **82**, 2294 (1999).
63. J. M. Kincaid, G. Stell, and C. K. Hall, *J. Chem. Phys.* **65**, 2161 (1976).
64. E. A. Jagla, *J. Phys. Condens. Mater.* **11**, 10251 (1999).
65. M. R. Sadr-Lahijany, A. Scala, S. V. Buldyrev, and H. E. Stanley, *Phys. Rev. Lett.* **81**, 4895 (1998).
66. G. Malescio, G. Franzese, A. Skibinsky, S. V. Buldyrev, and H. E. Stanley, *Phys. Rev. E* **71**, 061504 (2005).
67. P. G. Debenedetti, V. S. Raghavan, and S. S. Borick, *J. Phys. Chem.* **95**, 4540 (1991).
68. P. Kumar, G. Franzese, and H. E. Stanley, *Phys. Rev. Lett.* **100**, 105701 (2008).
69. G. D'Arrigo, G. Maisano, F. Mallamace, P. Migliardo, and F. Wanderlingh, *J. Chem. Phys.* **75**, 4264 (1981).
70. A. Scala, F. W. Starr, E. La Nave, F. Sciortino, and H. E. Stanley, *Nature* **406**, 166 (2000).
71. Z. Yan, et al., *Phys. Rev. Lett.* **95**, 130604 (2005); Z. Yan, et al., *Phys. Rev. E* **73**, 051204 (2006); Z. Yan, et al., *Phys. Rev. E* **76**, 051201 (2007); Z. Yan, et al., *Phys. Rev. E* **77**, 042201 (2008).
72. N. Giovambattista, P. J. Rossky, and P. G. Debenedetti, *Phys. Rev. E* **73**, 041604 (2006).
73. P. H. Poole, T. Grande, C. A. Angell, and P. F. McMillan, *Science* **275**, 322 (1997).
74. J. L. Yarger and G. H. Wolf, *Science* **306**, 820 (2004).
75. F. Mallamace, et al., *J. Chem. Phys.* **124**, 161102 (2006).
76. G. W. Robinson, S.-B. Zhu, S. Singh, and M. W. Evans, *Water in Biology, Chemistry, and Physics: Experimental Overviews and Computational Methodologies*, World Scientific, Singapore, 1996.
77. J. Horbach and W. Kob, *Phys. Rev. B*, **60**, 3169 (1999).
78. F. X. Prielmeier, E. W. Lang, R. J. Speedy, and H. D. Lüdemann, *Phys. Rev. Lett.* **59**, 1128 (1987).
79. K. Ito, C. T. Moynihan, and C. A. Angell, *Nature* **398**, 492 (1999).
80. J. Swenson, H. Jansson, W. S. Howells, and S. Longeville, *J. Chem. Phys.* **122**, 084505 (2005).
81. I. Saika-Voivod, P. H. Poole, and F. Sciortino, *Nature* **412**, 514 (2001).
82. D. C. Rapaport, *The Art of Molecular Dynamics Simulation*, Cambridge University Press, Cambridge, 1995.
83. F. H. Stillinger and A. Rahman, *J. Chem. Phys.* **57**, 1281 (1972).
84. W. Götze and L. Sjögren, *Rep. Prog. Phys.* **55**, 241 (1992).
85. P. H. Poole, I. Saika-Voivod, and F. Sciortino, *J. Phys. Condens. Mater.* **17**, L431 (2005).

86. P. Kumar, F. W. Starr, S. V. Buldyrev, and H. E. Stanley, *Phys. Rev. E* **75**, 011202 (2007).
87. S.-H. Chen, et al., *Proc. Natl. Acad. Sci. USA* **103**, 12974 (2006).
88. F. Mallamace, et al., *Proc. Natl. Acad. Sci. USA* **104**, 424 (2007).
89. P. Kumar, et al., *Phys. Rev. Lett.* **97**, 177802 (2006).
90. S.-H. Chen, et al., *Proc. Natl. Acad. Sci. USA* **103**, 9012 (2006).
91. D. Liu, et al., *Proc. Natl. Acad. Sci. USA* **104**, 9570 (2007).
92. D. A. Fuentevilla and M. A. Anisimov, *Phys. Rev. Lett.* **97**, 195702 (2006).
93. K. Morishige and K. Nobuoca, *J. Chem. Phys.* **107**, 6965 (1997).
94. A. Schreiber, I. Ketelsen, and G. H. Findenegg, *Phys. Chem. Chem. Phys.* **3**, 1185 (2001).
95. K. Overloop and L. Van Gerven, *J. Magn. Res. Ser. A* **101**, 147 (1993).
96. N. Bloemberger, E. M. Purcell, and R. V. Pound, *Phys. Rev.* **73**, 679–712 (1948).
97. O. Mishima, *J. Chem. Phys.* **100**, 5910 (1994).
98. L. Liu, A. Faraone, and S.-H. Chen, *Phys. Rev. E* **65**, 041506 (2002).
99. M. D. Ediger, *Ann. Rev. Phys. Chem.* **51**, 99 (2000).
100. K. L. Ngai, J. H. Magill, and D. J. Plazek, *J. Chem. Phys.* **112**, 1887 (2000).
101. R. Yamamoto and A. Onuki, *Phys. Rev. Lett.* **81**, 4915 (1998).
102. L. Bosio, S.-H. Chen, and J. Teixeira, *Phys. Rev. A* **27**, 1468 (1983).
103. G. E. Walrafen, *J. Chem. Phys.* **47**, 114 (1967); G. E. Walrafen, et al., *Chem. Phys.* **85**, 6970 (1986).
104. G. D'Arrigo, G. Maisano, F. Mallamace, P. Migliardo, and F. Wanderlingh, *J. Chem. Phys.* **75**, 4264 (1985).
105. C. G. Venkatesh, S. A. Rice, and J. B. Bates, *J. Chem. Phys.* **63**, 1065 (1975); T. C. Sivakumar, S. A Rice, and M. G. Sceats, *J. Chem. Phys.* **69**, 3468 (1978).
106. F. Mallamace, et al., *Proc. Natl. Acad. Sci. USA* **104**, 18387 (2007).
107. R. S. Smith, C. Huang, and B. D. Kay, *J. Phys. Chem. B* **101**, 6123 (1997).
108. M. A. Floriano, Y. P. Handa, D. D. Klug, and E. Whalley, *J. Chem. Phys.* **91**, 7187 (1989).
109. K. Modig, B. Pfrommer, and B. Halle, *Phys. Rev. Lett.* **90**, 075502 (2003).
110. P. Kumar, *Proc. Natl. Acad. Sci. USA* **103**, 12955 (2006).
111. C. Bennemann, C. Donati, J. Baschnagel, and S. C. Glotzer, *Nature* **399**, 246 (1999).
112. S. Whitelam, L. Berthier, and J. P. Garrahan, *Phys. Rev. Lett.* **92**, 185705 (2004).
113. A. Zürcher and T. Keyes, *Phys. Rev. E* **55**, 6917 (1997).
114. D. J. Wales, *Energy Landscapes*, Cambridge University Press, Cambridge, 2003.
115. E. Tombari, C. Ferrari, G. Salvetti, and P. G. Johari, *Phys. Rev. B* **77**, 0242304 (2008).
116. F. H. Stillinger, *Science* **225**, 983 (1984); F. H. Stillinger, *Science* **267**, 1935 (1995).
117. S. Sastry, P. G. Debenedetti, and F. H. Stillinger, *Nature* **393**, 554 (1998).
118. M. Nicodemi and A. Coniglio, *Phys. Rev. Lett.* **82**, 916 (1999).
119. N.O. Birge and R.S. Nagel, *Phys. Rev. Lett.* **54**, 2674 (1985).
120. E. Tombari, C. Ferrari, G. Salvetti, and J. P. Johari, *J. Chem. Phys.* **130**, 124505 (2009).
121. C. A. Angell, *Ann. Rev. Phys. Chem.* **34**, 593 (1983).
122. C. A. Angell, *Science* **319**, 582 (2008).
123. C. A. Angell, *Science* **267**, 1924 (1995).
124. E. Tombari, C. Ferrari, and G. Salvetti, *Chem. Phys. Lett.* **300**, 749 (1999).

125. T. Takamuku, et al., *J. Phys. Chem. B* **101**, 5370 (1997).
126. E. W. Hansen, H. C. Gran, and E. J. Sellevold, *J. Phys. Chem. B* **101**, 7027 (1997).
127. E. Tombari, C. Ferrari, and G. Salvetti, *J. Chem. Phys.* **122**, 104712 (2005).
128. S. Maruyama, K. Wakabayashi, and M. Oguni, *AIP Conf. Proc.* **708**, 675 (2004).
129. M. Oguni, S. Maruyama, K. Wakabayashi, and A. Nagoe, *Chem. Asian J.* **2**, 514 (2007).
130. G. Ferrari, G. Salvetti, E. Tombari, and G. P. Johari, *Phys. Rev. E*, **54**, R1058 (1996).
131. H. Fujimori and M. Oguni, *J. Phys. Chem. Solids* **54**, 271 (1993).
132. M. Oguni, Y. Kanke, and S. Namba, *AIP Conf. Proc.* **982**, 34 (2004).
133. F. Mallamace, et al., *Proc. Natl. Acad. Sci. USA* **105**, 12725 (2008).
134. M. Matubayasi, C. Wakai, and M. Nakahara, *Phys. Rev. Lett.* **78**, 2573–2576 (1997).
135. K. Modig, B. G. Pfrommer, and B. Halle, *Phys. Rev. Lett.* **90**, 075502 (2003).
136. K. Modig and B. Halle, *J. Am. Chem. Soc.* **124**, 12031–12041 (2002).
137. J. C. Hindman, *J. Chem. Phys.* **44**, 4582–4592 (1966).
138. E. M. Purcell, H. C. Torrey, and R. V. Pound, *Phys. Rev.* **69**, 37–38 (1946).
139. F. Bloch, *Phys. Rev.* **70**, 460–474 (1946).
140. A. Abragam, *The Principles of Nuclear Magnetism*, Clarendon, Oxford, 1961.
141. C. A. Angell, J. Shuppert, and J. C. Tucker, *J. Phys. Chem.* **77**, 3092–3099 (1973).
142. B. G. Pfrommer, F. Mauri, and S. G. Louie, *J. Am. Chem. Soc.* **122**, 123–129 (2000).
143. H. E. Stanley, et al., *Physica A* **386**, 729–743 (2007).
144. P. Kumar, et al., *Proc. Natl. Acad. Sci. USA* **104**, 9575 (2007).
145. L. Xu, et al., *Nature Physics* **5**, 565–569 (2009).
146. M. G. Mazza, N. Giovambattista, F. W. Starr, and H. E. Stanley, *Phys. Rev. Lett.* **96**, 057803 (2006).